AN INTEGRATED SYSTEM FOR ROAD CONDITION AND WEIGH-IN-MOTION MEASUREMENTS USING IN-PAVEMENT STRAIN SENSORS

A Dissertation
Submitted to the Graduate Faculty
of the
North Dakota State University
of Agriculture and Applied Science

By

Zhiming Zhang

In Partial Fulfillment of the Requirements
for the Degree of
DOCTOR OF PHILOSOPHY

Major Department:
Civil and Environmental Engineering

July 2016

Fargo, North Dakota

North Dakota State University
Graduate School

Title

AN INTEGRATED SYSTEM FOR ROAD CONDITION AND WEIGH-IN-MOTION MEASUREMENTS USING IN-PAVEMENT STRAIN SENSORS

By

Zhiming Zhang

The Supervisory Committee certifies that this ***disquisition*** complies with North Dakota State University's regulations and meets the accepted standards for the degree of

DOCTOR OF PHILOSOPHY

SUPERVISORY COMMITTEE:

Dr. Ying Huang
Chair

Dr. Amiy Varma

Dr. Raj Bridgelall

Dr. Jerry Gao

Approved:

August 8, 2016
Date

Dr. Dinesh Katti
Department Chair

ABSTRACT

The United States has the world's largest road network with over 4.1 million miles of roads supporting more than 260 million of registered automobiles including around 11 million of heavy trucks. Such a large road network challenges the road and traffic management systems such as condition assessment and traffic monitoring. To assess the road conditions and track the traffic, currently, multiple facilities are required simultaneously. For instance, vehicle-based image techniques are available for pavements' mechanical behavior detection such as cracks, high-speed vehicle-based profilers are used upon request for the road ride quality evaluation, and inductive loops or strain sensors are deployed inside pavements for traffic data collection. Having multiple facilities and systems for the road conditions and traffic information monitoring raises the cost for the assessment and complicates the process. In this study, an integrated system is developed to simultaneously monitor the road condition and traffic using in-pavement strain-based sensors, which will phenomenally simplify the road condition and traffic monitoring. To accomplish such a superior system, this dissertation designs an innovative integrated sensing system, installs the integrated system in Minnesota's Cold Weather Road Research Facility (MnROAD), monitors the early health conditions of the pavements and ride quality evaluation, investigates algorithms by using the developed system for traffic data collection especially weigh-in-motion measurements, and optimizes the system through optimal system design. The developed integrated system is promising to use one system for multiple purposes, which gains a considerable efficiency increase as well as a potential significant cost reduction for intelligent transportation system.

ACKNOWLEDGEMENTS

First, I wish to thank my academic advisor Dr. Ying Huang for her academic guidance and support during my study. Also, I would like to thank my committee members: Dr. Amiy Varma from Civil and Environmental Engineering Department, Dr. Raj Bridgelall from Upper Great Plains Transportation Institute (UGPTI), and Dr. Zhili (Jerry) Gao from Construction Management and Engineering Department.

Furthermore, I would like to thank the engineers and staffs at MnROAD facility, MnDOT, for supplying the needed facilities used in this study. Also, I would like to thank the Civil and Environmental Engineering Department at NDSU, Upper Great Plains Transportation Institute (UGPTI), Mountain-Plains Consortium (MPC), and the US Department of Transportation (USDOT) for financial support during this research.

Finally, thanks for all the team research members in CEE Sensors Infrastructure Lab: Xiao Liang, Leonard Chia, Fodan Deng, and Mu'ath Al-Tarawneh, who helped the author during his work to complete this study. I would like to extend my gratitude to all my families in China who kept caring and supporting during my progress.

DEDICATION

I dedicate this work to my dear wife Yanmei Xie for her endless support and understanding.

I dedicate this work to my mentor and friend Professor Kaifeng Zheng at Southwest Jiaotong University in China.

Final dedication to my dear parents and siblings for their deep concern and caring.

TABLE OF CONTENTS

LIST OF TABLES

LIST OF FIGURES

LIST OF ABBREVIATIONS

ASTM .....American Society for Testing and Materials

HSRI .....Highway Safety Research Institute

MnROAD.....Minnesota's Cold Weather Road Research Facility

MnDOT.....Minnesota Department of Transportation

USDOT .....U.S. Department of Transportation

UGPTI.....Upper Great Plains Transportation Institute

MPC .....Mountain-Plains Consortium

SNR.....Signal to Noise Ratio

ESAL.....Equivalent Single Axle Load

IRI .....International Roughness Index

RIF .....Road Impact Factor

EAR.....Ensemble Average RIF

WIM.....Weigh in Motion

FBG.....Fiber Bragg Grating

GFRP.....Glass Fiber Reinforce Polymer

IFFT .....Inverse Fast Fourier Transform

PSD .....Power Spectral Density

EMI .....Electromagnetic Interference

A/D.....Analog to Digital

LIST OF SYMBOLS

n.....Index of refraction

Λ.....Grating periodicity of the FBG

v.....Average vehicle travelling speed

P_L.....Linear load function

B_ω.....Signal bandwidth in angular frequency

F_S.....Nyquist sampling rate

$1-\eta$.....Strain transfer coefficient

f_c.....Cutoff frequency of digital filter

$S_\xi(\kappa_0)$.....PSD at κ_0 or initial PSD in m^3/cycle

R_{weight}.....Resolution of sensor in the unit of weight

$N_{bits\_effective}$.....Effective analog-to-digital (A/D) converter bits

S_A.....Axle spacing

B_f.....Fractional noise equivalent bandwidth

N_{reddB}.....Noise reduction in dB

E_{weight}.....Equivalent weight error

1. INTRODUCTION

The United States has more than 4.1 million miles of roads, including the interstate highway system. These roads support more than 260 million of registered automobiles driving on them including around 11 million of heavy trucks [1]. With such a huge road network and such a vast automobile system, it is an extremely challenging task to monitor and maintain the superior condition of the roads and the smooth traffic on the roads. Currently, separate systems for pavement condition evaluations, roughness measurements, and traffic data collections such as weigh-in-motion collections exist. However, an integrated system which can simultaneously monitor the pavement conditions, roughness of the roads, and the weigh-in-motion of the passing vehicles is yet developed.

1.1. Pavement Condition Monitoring

Statistics published by the Federal Highway Administration indicates that maintenance and rehabilitation of highway pavements in the United States requires over $17 billion a year [1]. Conventional visual and manual pavement distress analysis approaches as shown in Figure 1 in which the inspectors traverse the roads and stop and measure the distress objects when they are found are very costly, time-consuming, dangerous, labor-intensive, tedious, and subjective. In additions, these approaches have high degree of variability, are unable to provide meaningful quantitative information, and almost always lead to inconsistencies in distress detail over space and across evaluations [2].

Figure 1. Manual pavement distress measurements [3].

Thus, to solve the challenges of the manual pavement condition assessment and evaluate the performance of pavement structures more accurately, consistently, and safely, in-pavement sensing technologies are necessary. Traditionally, electrical sensors such as electrical strain gauges and electromagnetic sensors are commonly applied for pavement condition evaluation. In recent decades, fiber optic sensors, due to their unique advantages of compactness, immunity to EMI and moisture, capability of quasi-distributed sensing, and long life cycle, generate numerous attentions for its applications in pavement condition monitoring as well.

1.1.1. Electrical sensors

Electrical sensors convert the change of a physical parameter to an electrical signal. For pavement condition monitoring, the transducer in electrical sensors converts the mechanical, thermal, or other form of energy in pavements such as strain, stress, and temperature to electrical energy. The application of electrical sensors in pavement monitoring can be traced back to the 1960s [4].

In early 1990s, Sebaaly et al. [5] tested various types of pavement instrumentation, including pressure cell, deflectometer, strain gauge, thermocouple, moisture sensor, and

transverse vehicle location sensor, for field evaluation under actual truck loading. In 1995, Sebaaly et al. [6] measured the tensile strains in flexible pavements using the Hall Effect sensors in an H-gage configuration. In 2001, commercial diaphragm-type stress cells were embedded in the subgrade of pavements to compare the performance of two instrumented pavement test sections under linear traffic simulator [7]. In 2005, Huff et al. [8] investigated piezoelectric axle sensors to obtain dynamic pavement deflection data. In 2011, Xue and Weaver [9] explored the effect of wide-base tire on pavement strain response based on the data collected from SPS-8 on Ohio-SHRP U.S. 23 Test Road in 1997. Recently, self-powered wireless sensor was also developed based on the integration of piezoelectric transduction with floating-gate injection, which is capable of detecting strain and temperature simultaneously [10].

These electrical sensors, despite of the relatively low cost, have some significant limitations, indicating that they are unreliable for long-term pavement performance monitoring. For example, these sensors have shown high susceptibility to electromagnetic interference (EMI) and relatively short life cycles. Furthermore, corrections are needed due to temperature variations, and lead wires/connections are easily degraded by high humidity in the pavement environment.

1.1.2. Optical fiber sensors

To overcome the shortcomings of the electrical sensors, advanced fiber optic sensing technologies have been developing rapidly. Among various fiber optic sensors, the optical fiber Bragg grating (FBG) sensor, which is the most common engineering-applied fiber optic sensor, has been investigated widely for structural health monitoring of various infrastructures [11-14]. Because of its distributed sensing capabilities, light weight, immunity to electromagnetic interference, strong survival ability, and high accuracy and sensitivity [15, 16], FBG sensor is a

potential candidate for long-term pavement performance evaluation. The bare FBG sensors for pavement monitoring has been investigated by Wang and Tang [17] in 2005 using a pair of fiber gratings for simultaneous measurement of strains and temperatures within pavements.

However, a bare FBG sensor, which is made of glass, is very easily damaged during the harsh pavement construction process [18]. Glass fiber reinforced polymer (GFRP) material, on the other hand, has proven to be a strong material for civil applications and has been used to package and protect FBG sensors to improve their ruggedness [19, 20]. The innovation of GFRP-FBG sensor enables potentials for a reliable fiber optic sensor for long-term pavement condition monitoring.

1.1.3. Pavement research facilities

To promote the developments of various instrumentation techniques for pavement monitoring purpose and pavement material studies, the U. S. transportation departments and agencies set up pavement research facilities (test roads) in some of the states. The foremost was the AASHO Road Test conducted in Ottowa, Illinois from 1958 to 1960 [21]. The National Center for Asphalt Technology (NCAT) at Auburn University established test tracks in Opelika, AL since 1986. In 2004, eight sections of the NCAT test tracks were fully instrumented to measure in situ pavement responses under load [21]. In Minnesota, the Cold Weather Road Research Facility in Minnesota (MnROAD) of Minnesota Department of Transportation (MnDOT) was heavily instrumented with 40 test cells. Based on the monitored data from MnROAD facility, Lukanen developed mechanistically based load equivalency factors (LEF) in 2005 for pavement design [22]. In Virginia, Smart Road facility in Blacksburg of Virginia was also instrumented its twelve sections for pavement related studies [23]. In 2006, Loulizi et al. [24] used one of the instrumented sections of the Virginia Smart Road to compare the difference

between theoretical and experimental stresses and strains measured in situ of a flexible pavement section.

Although instrumented road sections have extensive values for self-monitoring, due to the potential high cost associated with the instrumented road sections, they are mostly limited to research facilities. Further efforts are still in needs to extend the instrumentations to real-time traffic roads.

1.2. Road Roughness Condition Monitoring

As an alternative to instrumentations in pavements, for a more mobile road condition assessment for maintenance resource allocation, roughness obtained through inertial road profiling method as shown in Figure 2 has been long used as one of the major criteria as a global measure of roadway serviceability.

Figure 2. Standard road profiling for roughness measurements [25].

The ASTM E867 standard defines roughness as “the deviation of a surface from a true planar surface with characteristic dimensions that affect vehicle dynamics and ride quality” [26]. Pavement roughness adversely affects vehicle wear, ride quality, and transportation safety [27-

30]. The higher dynamic axle loading from roughness accelerates pavement deterioration [31]. Rough roads can also increase fuel consumption by as much as 4-5 percent [32].

1.2.1. Roughness index

Researchers proposed many different roughness statistics to describe the severity of pavement roughness including the international roughness index (IRI) and the power spectral density (PSD) method. However, the IRI is the most commonly used index for roughness evaluation [33]. The IRI computation relies on a mathematical model called a quarter-car model. This model simulates the response of a serially coupled damped mass-spring system to estimate the vertical motions of equivalent wheel-assembly masses. The IRI is the accumulated absolute rate difference between the simulated sprung- and unsprung mass motions per unit of distance travelled.

Another important characterization of roughness is the power spectral density (PSD). It is a mathematical representation of the spatial wavelength composition of road profiles rather than a summary index of roughness [34]. Researchers found that most pavement profiles such as road and runway surfaces have very similar PSD shapes. This observation has led to the use of coefficients that fit exponential functions to the PSD shapes as alternative summaries of roughness.

Less frequently used methods also exist. These include the profile index method which is the root-mean square of a band-pass filtered road profile [35], the ride number method which is a transformation of the elevation profile per the ASTM E-1489 standard [36], and the root mean square of vertical acceleration approach which is a statistic method based on the rate of the grade change of the longitudinal profile [37].

1.2.2. Roughness measurement methods

The methods for roughness measurements fall into three major classes [38]. Class I uses the traditional longitudinal surveys by rod and level or by some other laborsaving apparatus that requires walking along the test path. The Class II techniques measure the road profile with various types of profilometers such as the Chloe-type rolling straightedge [38]. Class III is an indirect measuring method described as a response-type road roughness meters (RTRRM) that most highway agencies used until the mid-1980s or as an inertial road profilers that began in the 1960s [39]. The RTRRM devices measure the response of the vehicle to the road profile using transducers to accumulate the vertical movement of the axle with respect to the vehicle's body. This method directly reflected the users' ride quality experience. However, variations in suspension characteristics and speed result in measurement inconsistencies. Such approaches also do not provide a sample of the pavement longitudinal profile for spectral analysis.

The inertial road profiling methods use instrumented vehicles to collect road roughness data [40]. Inertial profilers collect pavement condition data at highway speeds and record sufficient data to evaluate the spectral content of the pavement profile. This benefit has led to a substantial increase of countries adopting the method. The principal components of a high-speed profiler include laser-based height sensors, accelerometers and an accurate distance measuring system. The height sensors record the distance from the base of the vehicle to the pavement surface. Accelerometers above the height sensors record the vertical acceleration of the sensor to correct for reference plane bounces. In theory, double integration of the vertical acceleration signal would recover the vertical displacement of the vehicle. Practically, however, noise and initial conditions tend to create additional issues that limit their use in urban and local roads where the profiling vehicle must travel at low speeds and accommodate stop-and-go conditions

[41]. Nevertheless, in more ideal settings such as freeways, the inertial profiler equipment produces a longitudinal profile of the pavement from the two height measurements. In addition to the profilers, recently, some other more cost-effective approaches have been investigated to collect the acceleration data for roughness measurement using connected vehicles through vehicle-integrated inertial and geospatial position sensors as well [27, 28].

According to NCHRP Report 334 [42], most transportation agencies now collect pavement roughness data using the automated systems mentioned above, especially the inertial profilers, for at least part of their paved roadway network. The inertial road profiling method for roughness measurements requires specially trained technicians and facilities including laser-based height sensors, accelerometers and an accurate distance measuring system, which possess high cost for its use. The literature has very little information about the cost of using such inertial profilers. One study reported pavement profile data collection and analysis costs in the range of $2.23 - $10.00/mile with an average cost of $6.12/mile [43]. In general, the relatively high expense and labor requirements of existing approaches prevent agencies from monitoring large portions of their roadway network more often than once annually. Thus, they often make maintenance and rehabilitation decisions based on outdated roughness data. In addition, infrequent roughness measurements preclude the identification of dangerous distress symptoms such as frost heaves that appear and disappear between annual monitoring cycles. These situations result in roadway safety gaps that increase liability.

1.3. Weigh-In-Motion

Sustained economic development has led to a large increase in roadway transportation. Traffic loads play a critical role in the performance and deterioration of pavements. Hence, the weight of heavy vehicles has been a critical factor in the design and maintenance of roads. The

American Association of State Highway and Transportation Officials (AASHTO) pavement design guide uses the concept of equivalent single axle load (ESAL) to account for the accumulation of traffic load [44]. In 2005 the National Cooperative Highway Research Program (NCHRP) of the Transportation Research Board (TRB) proposed the load spectra to describe the traffic load [45]. All of these methods rely on the availability of practical real-time solutions to measure the volume and weight of vehicles traversing specific road segments.

1.3.1. Static weight scales

The traditional practice of measuring vehicle weight is to install static weight scales in weight stations alongside the roadways. The heavy vehicles are directed to stop on the static weight scale in a weight station. The static scales typically achieve accuracies of 1% to 5%. Weight stations are required in most highway systems for weight control of the roads and bridges in the road system.

The static scales, although high accuracy, have several limitations such as diminishing roadway capacity by interrupting traffic flows, and the process of stopping and measuring creating a throughput bottleneck. Consequently, traffic enforcement officers will allow potentially overweight vehicles to bypass the weight station when the queue extends to the main line. Hence, weigh-in-motion (WIM) systems became a popular alternative to the static scale.

1.3.2. Weigh-in-motion technology

A WIM system consist of a device that measures the dynamic axle weight of a moving vehicle to estimate the corresponding static axle mass [46]. Compared with static scales, WIM technology has gain popularity because of its ability to collect continuous traffic data without human intervention. Since the concept of WIM was brought up sixty years ago [47], WIM technologies have been used increasingly around the world for weight control of heavy vehicles,

the protection and management of pavement and other infrastructures [48]. In fact, most of the weight stations in United States use slow-speed WIM sensors that can estimate the weight of a vehicle that is moving at speeds up to 15mph. For example, there are more than 100 Weigh-in-Motion stations throughout California by 2002 [49]. The original highway WIM system [50] used weighing devices in one lane of the road.

The introduction of weight-station bypass programs such as Pre-Pass encourages the development of high-speed WIM sensors. As early as 1989 [51], a high speed WIM system which was manufactured and supplied by International Road Dynamics (IRD), was installed on Highway 1 near Regina of Canada. When installed as in-pavement sensors, such high-speed WIM devices can enable real-time traffic monitoring, weight-based tolling, and traffic flow prediction, all of which are critical measures that nearly all transportation activities require [52]. During the past twenty years, both low-speed and high-speed WIM stations have been widely studied and developed by worldwide scholars and transportation agencies.

For WIM measurements, many in-pavement sensing systems were developed including the piezoelectric sensors, bending plate, load cell, and fiber optic sensor [53]. Currently, most of the available WIM systems rely on strain measurements or can be transferred to strain measurements as a basis for weight calculation. Piezoelectric sensors, made from polarized crystal that generates an electric charge when mechanically deformed, can be used for permanent applications when installed directly into a road slot or for portable applications when taped down. Bending plate WIM system, attached with strain gauges underside, measures the dynamic load as a vehicle passes over. The data is then calibrated to obtain the vehicle's static load. Load cell WIM system needs to be installed with a concrete vault. It has a single load cell with two

scales, each of which measures the either the left or right axle load. The summation of the measurements from the two scales produces the total axle weight.

Due to the distributed sensing properties, high environment resistance, and other advantages, the studies and applications of optic fiber sensors in WIM systems increased significantly in the past 10 years [54-58]. A fiber optic sensor, made of two metal strips welded around an optical fiber, measures the load applied on the fiber based on the glass fiber's photo-elastic property that the pressure transferred to the optical fiber creates a phase shift between both polarization modes, i.e. a faster vertical mode and a slower horizontal mode. In 2007, Cheng et al. [53] presented the design of a capacitive flexible weighing sensor for a vehicle WIM system and Zhang et al [59] investigated a WIM system based on multiple low cost, light weight, small volume and high accuracy embedded concrete fiber optic strain sensors. To date, the WIM system based on the fiber optic sensors are still limited.

1.3.3. Weigh-in-motion sampling frequency

To measure the high-speed WIM accurately using any in-pavement strain based sensors, it requires an appropriate sampling frequency for a specific traveling speed. Insufficient sampling reduces the measurement accuracy. On the other hand, excessive sampling reduces the potential for real-time measurements by requiring more computational capability and memory space than is necessary [60]. In 1991, Loshbough et al. investigated the appropriate sampling rate for WIM measurements and determined that the sampling rate should be at least twice the natural resonant frequency of the scale weighing platform [61]. In 2009, Federal Highway Administration (FHWA) and New Jersey Department of Transportation (NJDOT) [62] tested WIM measurements under cyclic loading at a low speed using piezoelectric sensors. The test revealed a roughly 25% increase in voltage output when the sampling rate increased from 100Hz

to 1,000Hz but did not analyze the specific trade-off between sampling rate and accuracy. The recent attractiveness of high-speed WIM technology for truck weight enforcement has led to numerous studies and practices relating to sampling rate selection [62-65]. However, the current literature lacks analysis on the influence of sampling rate selection on accuracy to guide the requirements for data acquisition facilities.

1.4. Integrated Monitoring System

With the development of information technology and digitization, pavement monitoring has been integrated to other monitoring systems, such as bridge monitoring. Many bridges worldwide are closely monitored because of their economic importance and vulnerability to extreme loading and harsh environmental conditions. The monitoring of bridges is convenient to be integrated with pavement monitoring because of their similarity in structure and function. The monitoring system of Geumdang Bridge in Korea using high-resolution wireless sensors were combined together with the two-lane passing test road which employed 1,897 sensors to evaluate three types of pavement constructed along the road length [66]. In Hong Kong, the integrated monitoring system with more than 800 sensors permanently installed on the three long-span cable-supported bridges- the suspension Tsing Ma Bridge, the cable-stayed Kap Shui Mun Bridge, and the Ting Kau Bridge [67]. In United States, the Commodore Barry Bridge was instrumented using 77 sensors and 115 channels to track the loading environment and structural responses, and expected to be integrated with a WIM system in the future [67]. In 2012, Kim and Lynch [68] installed wireless sensors on both the bridge and moving vehicle and record the dynamic interaction between the bridge and vehicle. Although the pavement condition monitoring has been investigated to be integrated with the bridge condition detection, an

integrated system to simultaneous monitoring of road conditions and traffic such as WIM is yet to be developed.

1.5. Problem Statement and Research Objectives

From the literature review above, current challenges for pavement condition and traffic monitoring can be summarized below:

1) Although there are versatile electrical sensors existing for road condition monitoring such as strain gauges and piezo-electric sensing, the electrical sensors have some significant limitations, such as high susceptibility to electromagnetic interference (EMI) and relatively short life cycles, which prevent their applications for reliable long-term road condition evaluation. Due to the capabilities of immunity to EMI and high accuracy and sensitivity, fiber optic sensor is a potential candidate for long-term pavement performance evaluation. However, a bare fiber optic sensor made of glass is very easily damaged during the harsh pavement construction process, which needs to be improved for road condition monitoring;
2) As an alternative to in-pavement sensors, roughness index such as IRI can be used for a more mobile road condition assessment. Road roughness, which usually is obtained through inertial road profiling method, requires an individual automobile with instruments onboard to perform the roughness measurements, resulting in high measurement cost and preventing frequent road condition assessments;
3) On the other hand, the weight control on roads usually relies on static weight measurements from static scales in weight stations, which cannot meet the requirements for modern high-speed weight control. The WIM technologies can meet this challenge, however, the implantation of WIM system currently highly depends on

the experiences from the operating engineers and lacks guidance on its system design and sampling rate selections;

4) Literature reviews indicated that traditionally, pavement condition monitoring and traffic data collection require two specific systems: one automobile with instruments onboard for pavement condition evaluation and one instrumented weight station for weight control. Having multiple facilities and systems for the road conditions and traffic information monitoring raises the cost for the assessment and complicates the process.

To solve these challenges, the main objective of this dissertation is to develop an integrated system to simultaneously monitor the health condition of the roads and the WIM of passing vehicles, which will phenomenally simplify the road and traffic monitoring. The integrated system might have a great potential in future application because of its cost-efficiency and integrity. To achieve such an integrated system, the specific tasks in this study include:

1) Develop an integrated sensing system based on in-pavement strain sensors that is capable of serving the integrated road condition and traffic monitoring system;
2) Apply the integrated system for pavement condition monitoring and validate the system performance through field measurements;
3) Develop a method to apply the integrated system for road roughness monitoring and validate the methodology through numerical simulation and field testing;
4) Apply the integrated system for WIM measurements and develop guidance on the sampling requirements of the use of the system for high-speed WIM measurements;

5) Optimize the integrated system for optimal performance on road condition evaluation and high-speed WIM measurements considering real traffic.

1.6. Dissertation Organization

Based on the specific tasks aligned to achieve the main objective of this study above, this dissertation is divided into six chapters as follows: Chapter 2 describes the design of the integrated sensing system for road condition and WIM monitoring, its installation, and its field calibration; Chapter 3 presents the implementation of the integrated system for pavement health monitoring and roughness measurements; Chapter 4 introduces the application of the integrated system for WIM measurements and the design of the sampling optimization using such a system; Chapter 5 optimizes the system design for pavement condition and high-speed measurements using the integrated system; and Chapter 6 presents conclusions and recommended future work.

1.7. Premises and Delimitations

Premises form the basis upon which this research rests. In this study, there are two assumptions used throughout the dissertation: 1) The field validation in this study assumes that the target truck load is located right above the target sensor, so that the output of data collection and result analysis corresponds to the amount of imposed loading; and 2) For the system optimization in weigh-in-motion measurement, the input signal to noise ratio (SNR) of the A/D converter is equal to its output SNR. In practice, however, A/D devices may produce additional noise such that the output SNR is lower than the input SNR.

Delimitations define the scope of the research. In this study, we define three delimitations including: 1) The objects of this study on road condition and weigh-in-motion measurements are limited to concrete pavement panels that can be abstracted with a thin plate; 2) The numerical simulation and field validation in this study are based on the facilities available at MnROAD

research sections and this research doesn't include data collection or signal processing for real traffic; and 3) The field validation of roughness evaluation relies on the proportionality of RIF with IRI which was characterized by cited previous work for the accuracy of estimating the IRI from RIF measurements.

2. DESIGN AND CALIBRATION OF THE INTEGRATED SENSING SYSTEM

In this chapter, in-pavement strain sensors based on optical fiber Bragg grating are designed for the use of establishing an integrated sensing system for simultaneous road condition and traffic monitoring. The specifically designed in-pavement sensors were integrated as a sensing system and installed in an example concrete pavement for strain sensing calibration.

2.1. Design of the In-pavement Strain Sensors

As indicated in the literature review, it is desired for practical applications to have in-pavement strain sensors with capabilities of immunity to EMI, high accuracy, high sensitivity, and long-term reliability. Fiber Bragg grating (FBG) sensor, one type of fiber optic sensor, due to the advantages of possessing these capabilities mentioned above can be an alternative for long-term pavement performance evaluation. But the bare fiber optic sensor is made of glass and is easily to be damaged during pavement construction process. Glass fiber reinforced polymer (GFRP) material with great ruggedness has been considered as a potential packaging approach to protect FBG sensors for in-pavement installations [19, 20]. Thus, this study developed a rugged GFRP packaged FBG sensor for in-pavement strain sensing to achieve potential simultaneous road condition and traffic monitoring.

2.1.1. Operational principle of FBG sensors for strain sensing

FBG sensor, as one type of commonly used fiber optic sensors in civil engineering, is made by laterally exposing the core of a single-mode fiber to a periodic pattern of intense ultraviolet (UV) light as shown in Figure 3a for the operational principles. The UV light creates a fixed refractive index modulation, called grating. At each periodic refraction change, a small amount of light is reflected, forming a coherent large reflection at a particular wavelength known as the Bragg wavelength. Light signals at wavelengths other than the Bragg wavelength

propagate through the grating with negligible attenuation or signal variation. The ability to accurately preset and maintain the grating wavelength is a fundamental feature and advantage of fiber Bragg gratings [69]. Figure 3b shows a typical reflected spectrum of FBG. The Bragg wavelength satisfies the Bragg condition [70]:

$$\lambda_{Bragg} = 2n\Lambda \tag{1}$$

where n is the index of refraction and Λ is the grating periodicity of the FBG.

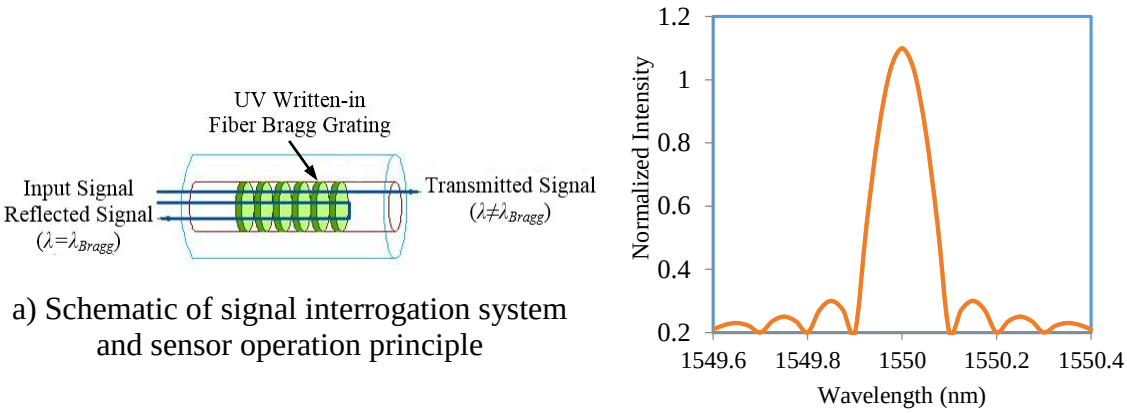

a) Schematic of signal interrogation system and sensor operation principle

b) Typical spectrum of FBG sensors

Figure 3. Sensor operation principle and typical spectrum [69].

Due to temperature and strain dependence of the parameter Λ, the wavelength of the reflected component will change as a function of temperature and/or strain. The general expression of the strain-temperature relationship for the FBG strain sensor and temperature compensation sensor, can be described as [69]

$$\frac{\Delta\lambda_1}{\lambda_1} = \frac{\Delta\lambda_\varepsilon}{\lambda} + \frac{\Delta\lambda_T}{\lambda_T} = (1-P_e)\varepsilon + (\alpha+\varsigma)\Delta T \tag{2}$$

where λ, ζ, α, P_e, ε, and T are the resonant wavelength, thermal-optics coefficient, thermal expansion coefficient, optical elasticity coefficient, strain, and temperature, respectively. The strain after temperature compensation can then be calculated as [69]:

$$\varepsilon = \frac{1}{(1-P_e)}\left(\frac{\Delta\lambda_1}{\lambda_1} - \frac{\Delta\lambda_T}{\lambda_T}\right) \quad (3)$$

2.1.2. Geometric design of the GFRP-FBG in-pavement strain sensor

To protect the FBG sensors from damaging during the construction process of the pavements, the GFRP packaged FBG sensors previously developed by Zhou [20] were modified and used in this study. The dimensions of the GFRP-FBG sensors were specifically designed for embedment in most concrete pavement panels. Two geometric layouts were designed for in-pavement strain sensing using GFRP-FBG sensors including one layout in three dimensions (3D) as shown in Figure 4a and one layout in one dimension (1D) as shown in Figure 4b. For the 3D GFRP-FBG strain sensor, the short-gauged sensor was intended to monitor the vertical strain and the long-gauged sensors were used to monitor the longitudinal and transverse strains inside pavements. The vertical sensor was designed and fabricated with a total height of 2.1 in. (5.33 cm), including the length of the GFRP holder, so that the size of the sensor is small enough to put inside most types of pavements. The longitudinal and transverse components of 3D sensors had a gauge length of 2.2 in. (5.59 cm). The diameter of 3D GFRP-FBG sensors was designed as 0.2 in. (0.51 cm). The 1D GFRP-FBG sensors had a longer gauge length of 3 in. (7.62 cm), and they shared the same diameter with 3D sensors. Figure 4 shows the detail geometric layout of the developed sensors.

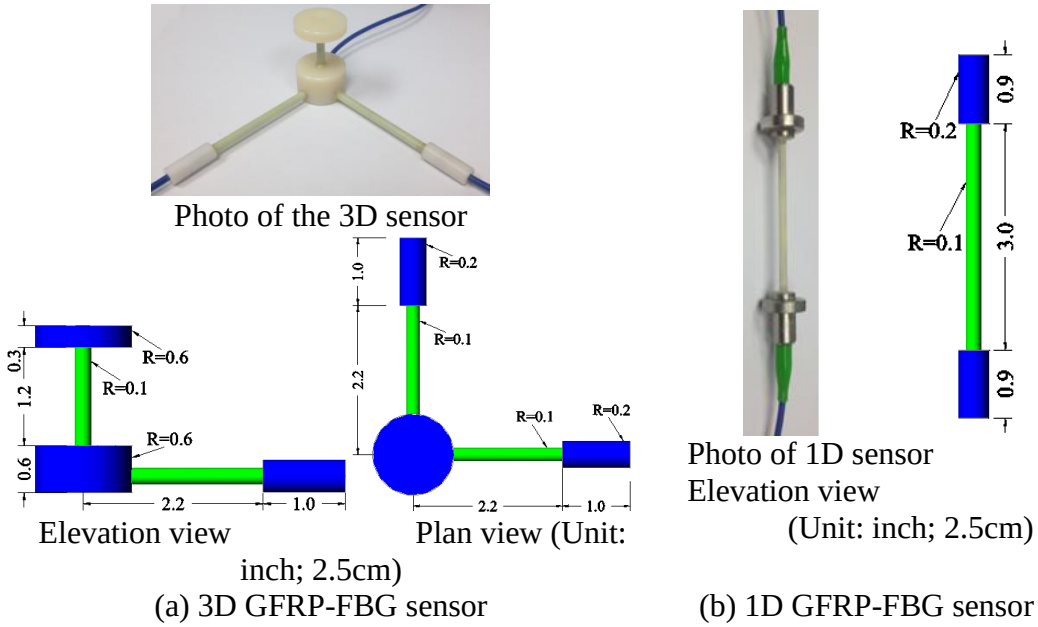

Figure 4. Geometric layout of the GFRP-FBG sensors.

The FBG signals from all of the strain sensors were monitored in real time using an optical signal analyzer (OSA) and recorded by computers for post processing. The NI PXIe-4844 Optical Sensor Interrogator was used in this research for FBG data acquisition. Sensor calibration followed the approaches used by Zhou [20]. The GFRP-FBG sensors had a strain sensitivity of 7.937×10^{-4} nm/με.

2.2. Design of the Integrated Sensing System

2.2.1. Implementation of an integrated sensing system

For simultaneous road condition and traffic monitoring, multiple GFRP-FBG sensors and other types of strain sensors may need to be installed inside pavements to form an integrated sensing system. Figures 5a and 5b illustrate the possible sensor implementation layouts which can achieve an integrated system. Inside each pavement section, four sensors are required including one 1D GFRP-FBG sensor, one 3D GFRP-FBG sensor, one strain gauge and one temperature sensor. The strain gauges, as shown in Figure 6 are needed for comparison, sensor

calibration, and backup for high-speed strain sensing in case the GFRP-FBG sensing instrument does not have sufficient sampling frequency. To assess the mechanical effect from traffic loading for WIM measurements, all in-pavement sensors are proposed to be implemented along the wheel path. If the pavements which the sensors to be installed is for new construction, all the GFRP-FBG sensors, strain gauges, and temperature sensor inside the overlay should be deployed at the bottom of the pavement layer. If installed inside existing pavement sections, channel cutting is required to hold the sensors on the bottom of the pavement sections and high performance polymer is recommended to apply inside the channels to bond the sensor to the existing pavements. The transmission connections of all the sensors are recommended to be protected and centrally connected to the instrument at the roadside for data acquisition and processing.

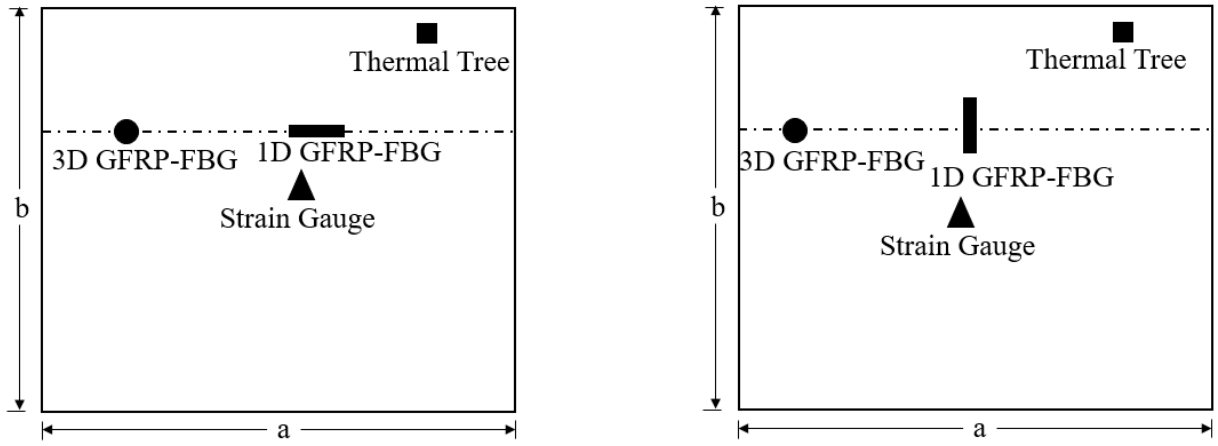

(a) Recommended layout #1 (b) Recommended layout #2

Figure 5. Recommended implementation layouts of the integrated sensing system. (Note: a and b are the length and width of the pavement panel.)

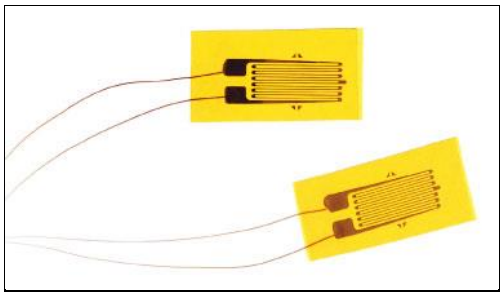

Figure 6. Strain gauges to be used in the integrated sensing system.

2.2.2. Example system implementation at MnROAD facility, MN

MnROAD facility, that supports this research, is owned and operated by the Minnesota Department of Transportation (MnDOT). MnROAD consists of two unique roadways including a two-lane low-volume road loop that is loaded with a 5-axle 80 000lb (36 287.39 kg) semi and the mainline, I-94's two westbound lanes using live traffic, as shown in Figure 7a. The example system implementation for this study utilized cell-40, which is an existing pavement test section (500 feet) on the low-volume road. Cell 40 originally had 15 ft. (4.57 m) by 12 ft. (3.66 m) skewed jointed concrete undoweled panels. After 19 years of continuous simulated truck loading, Cell 40 showed significant degradation. Two longitudinal cracks and one transverse crack were documented. Figure 7b shows the transverse crack and the short longitudinal crack, and Figure 7c shows the long longitudinal crack. The two longitudinal cracks were identified at 18 ft. (5.49 m) and 90 ft. (27.43 m) in lengths, while the transverse crack was at 12 ft. (3.66 m) at the east end of Cell 40. The long longitudinal crack occurred under the wheel path near the pavement edge, while the transverse crack and short longitudinal crack were located under the inner wheel path. The joint fault with an average width of a quarter inch (6.35 mm) was noticed with a history of pumping each spring. Based on the significant degradation, pavement rehabilitation was recommended by the MnDOT.

MnDOT installed a 3 in. (7.62 cm) ultra-thin fiber reinforced unbonded concrete overlay at MnROAD facility to cost-effectively rehabilitate the existing concrete pavements. The concrete material was reinforced with structural fibers of around 50% in weight. The overlay consisted of 6 ft. (1.83 m) by 6 ft. (1.83 m) square jointed panels, and sealed joints were applied between the overlay panels. Figures 7b and 7c also show the panel layout for original and overlay panels as the skewed joints for the underlying original concrete and the smaller rectangular joints for the overlay joint pattern. Moreover, to investigate the effectiveness of the separation layers two different thickness of fabrics were used in the study. Cell-40 was split in two new test sections each consisting of 250 ft. (76.2 m) The first consisted of a thin fabric interlayer (Fabric #1, 8 oz (236.59 ml) about one-eighth inch (3.18 mm)) with the 3 in. (7.62 cm) concrete overlay, which was numbered as Cell 140 (west end). The second test section consisted of a standard fabric interlayer (Fabric #2, 15 oz (443.6 ml) about a quarter inch (6.35 mm)) with the same 3 in. (7.62 cm) concrete overlay, which was numbered as Cell 240 (east end). The goal of the two test cells were to better understand if a standard (15 oz (443.6 ml)) fabric could be used under very thin concrete overlays without causing too much deflection and cracking when compared to the thinner (8 oz (236.59 ml)) fabric that would deflect less in theory [71].

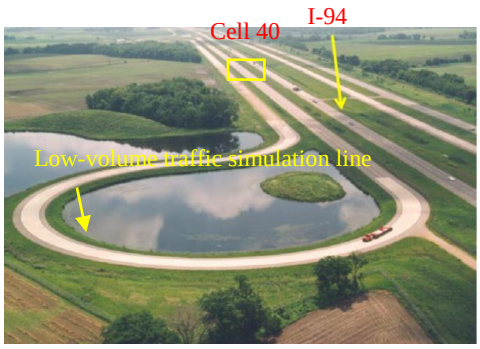

(a) Layout of MnROAD Facility [71]

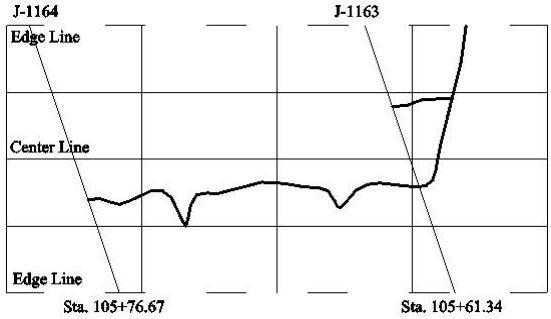

(b) Transverse and short longitudinal crack

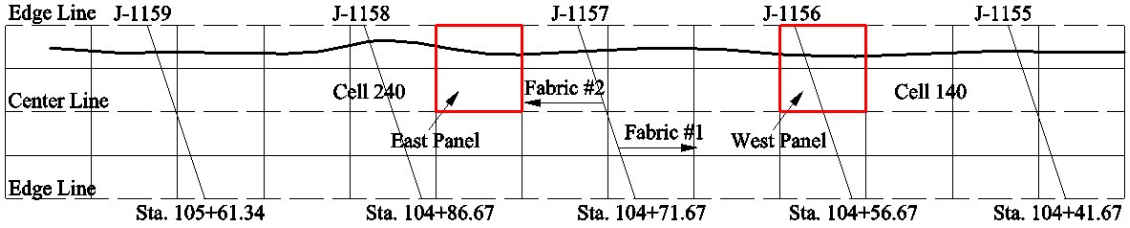

(c) Long longitudinal crack

Figure 7. MnROAD facility and cracking mapping of existing concrete pavements.

To calibrate and further validate the integrated system for simultaneous road condition and traffic monitoring, two panels in the concrete pavements of Cell 40 installed the recommended integrated sensing system. The panel with the first layout of a recommended integrated system as shown Figure 8a was named as West Panel of Cell 140 and the second layout of the recommended integrated system as shown in Figure 8b was named East Panel of Cell 240. Figures 8a and 8b illustrate the exact locations of the sensor layouts on the two panels with instrumented integrated systems, respectively, which were selected for monitoring based on the layout of the longer longitudinal crack and also the installation of fabric layers. To monitor the influence on the overlay from the joint opening behavior of the existing pavement, in addition to the required sensors for an integrated sensing system recommended in Figure 5, one more 1D-GFRP-FBG sensor (1D-3), was deployed across the joint of the existing pavement right

below the Sensor 1D-1. Figure 9a shows the installation of the Sensor 1D-3. In addition, to track the potential growth or shrinkage of the transverse crack, another additional longitudinal 1D GFRP-FBG sensor (1D-5) was implemented across the transverse crack as shown in Figure 9b. Also, another 1D GFRP-FBG sensor (1D-4) was placed inside the overlay above 1D-5 for comparison. All the GFRP-FBG sensors, strain gauges, and thermal trees inside the overlay were deployed 0.5 in. (1.27 cm) above the existing pavements for the convenience of installation and all the sensors were best aligned with the wheel path. High performance polymer was applied to bond the sensor to the existing concrete pavement. In addition, MnROAD also deployed traditional pavement sensors such as vibration wires for validations, which will be included in future study. The transmission connections of all the sensors were protected and centrally connected to the instrument at the roadside for data acquisition and processing.

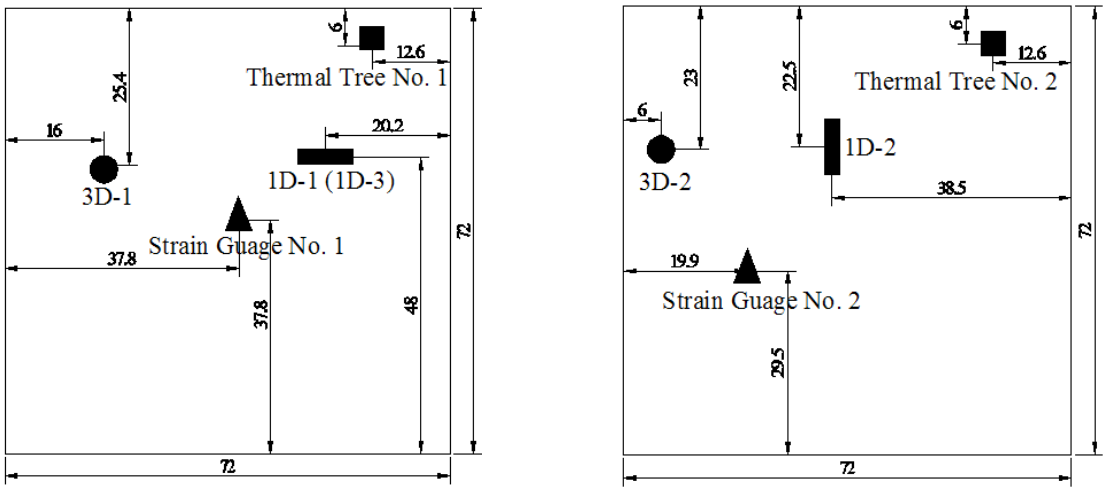

(a) West Panel in Cell 140 (b) East Panel in Cell 240

Figure 8. Sensor layouts on cell 40 (Unit: inch; 2.5cm). [Note: Sensor size not to scale.]

(a) Deployment of 1D-3 across the joint

(b) Deployment of 1D-5 across transverse cracks

Figure 9. Photos for sensor deployments in the existing pavement.

2.3. System Calibration

To calibrate the strain sensing performance of the developed integrated sensing system, field experiments were performed by loading the West Panel with instrumented sensing system using the wheels of the front two axles of the MnROAD 5-axle 80,000lb (36,287.39 kg) semi-truck as shown in Figure 10 a for its dimension and the axle weight distribution of the MnROAD truck. Figure 10 b shows a photo of the truck for demonstration. To measure strains induced from weights on top of in-pavement sensors, the tire must be directly loaded on the sensors. Due to the small size of a GFRP-FBG sensor or a strain gauge, the sensor only measures the strains induced by the load from one tire. Thus, for future axle weight measurements or WIM measurements based on the in-pavement strains measured by the sensors in this sensing system, one should multiply the number of tires of each axle for an estimation of axle weights. In this calibration, only one tire of a front axle of the MnROAD truck is used for the loading, considering the distribution of installed sensors. Since there are two tires in the front axle of the MnROAD truck, therefore, the loading on the GFRP-FBG sensor or strain gauge for calibration is half of the axle weight of 12 kips, which equals to 6 kips.

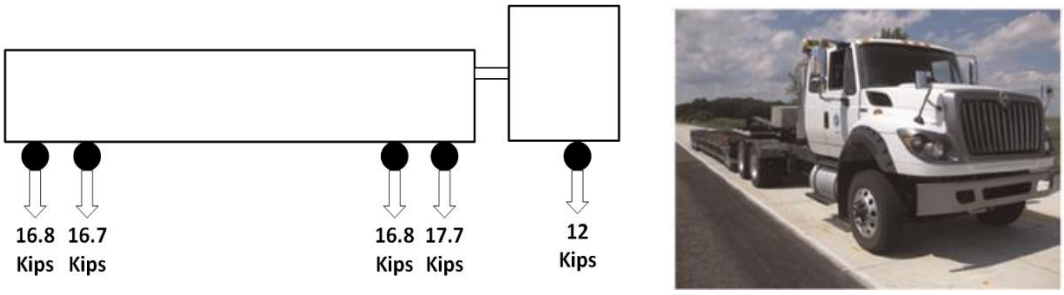

(a) Layout of MnROAD Truck (b) Photo of MnROAD Truck

Figure 10. Dimension of the MnROAD 5-axle semi-truck.

The data are collected using both the strain gauges and the GFRP-FBG sensors of the integrated system on the West Panel simultaneously. Table 1 shows the measured strains from the strain gauge and the transverse component of the 3D GFRP-FBG sensor, respectively. A maximum difference of 3.16% was noticed when comparing the test data from the strain gauge and that of the GFRP-FBG sensor, part of which can be accounted for by the positional difference between these two sensors. The variance within 5% proved the effectiveness of the developed GFRP-FBG sensor for strain sensing of the developed integrated sensing system. More importantly, Table 1 also shows that a 6kips of vehicle tire load of the front axle on top of a GFRP-FBG sensor embedded inside a concrete pavement will produce a strain of 62.07 με. Therefore, the load-strain sensitivity of the GFRP-FBG sensor is 10.3 με/kips, which is consistent with the studies performed by other researchers [72]. For weight measurements or WIM in following chapters, a load-strain sensitivity of 10.3 με/kips is then used based the calibration results here.

Table 1. Comparison between developed sensor and strain gauges.

Positions	Strain gauge (με)	3D-1-T (με)	Relative difference (%)
Axle #2	60.17	62.07	3.16%
Axle #1	52.46	51.18	-2.44%

2.4. Summary

This section presented an innovative robust integrated sensing system based on the newly developed GFRP-FBG sensors and strain gauges for future simultaneous road condition and traffic monitoring. The integrated system include an implementation of at least four sensors, including one 1D and 3D GFRP-FBG sensors, one strain gauges, and one temperature compensation sensor. The developed integrated sensing systems were deployed at MnROAD facility, MnDOT, for calibration. The developed sensors in the integrated system showed a 100% survival rate after the concrete overlay was cast in place. The comparison between the strain gauge data and the strain of developed GFRP-FBG sensor validated the reliability of the developed sensing technology for in-pavement strain sensing. The load-strain sensitivity of the GFRP-FBG sensor is calibrated to be 10.3 με/kips, which will be applied to all weight measurement purposes in following chapters.

3. PAVEMENT CONDITION ASSESSMENT AND ROAD ROUGHNESS EVALUATION

In this chapter, the developed integrated sensing system in Chapter 2 was applied in the example concrete pavement panels of MnROAD Cell 40 which also introduced in Section 2.2 and 2.3. The field case study is to validate the capability of the integrated sensing system for simultaneously monitoring of the pavement health condition and the road roughness situation. The monitored data can be further applied for road condition assessment and guide for resource relocations of road maintenance.

3.1. Pavement Condition Assessment Using the Integrated Sensing System

Strain distribution in pavements can provide valuable information for the pavement health conditions. With integrated sensing system instrumented, the measured strains from the system can be used to assess the pavement conditions effectively. This section details the early pavement performance assessment using the measured strains from the implemented integrated sensing system described in Chapter 2.

3.1.1. Early pavement performance evaluation

The concrete pavements described in Chapter 2 with integrated sensing systems instrumented were paved and cured for 21 days (June 10th 2013 to 1 July 2013). After curing, it was opened to simulated low-volume traffic with an 8 kips semi-truck as shown in Figure 10 driving 50 laps a day for 5 days each week. The early performance of the overlay for the first year was evaluated in this study. Table 2 shows the measured raw strains at 21 days (July 1st 2013, 100 ^{o}F (38 ^{o}C)), 52 days (August 1st 2013, 92 ^{o}F (33 ^{o}C)), 85 days (September 4th 2013, 88 ^{o}F (31 ^{o}C)), 162 days (November 22nd 2013, 22 ^{o}F (-6 ^{o}C), and 308 days (April 18th 2014, 34 ^{o}F (1 ^{o}C)) after paving. The accumulated strains, that were temperature compensated using equation (1) and with the consideration of strain transfer rate based on previous study [28], were

calculated by subtracting strains obtained at 21 days after paving from strains at 52 days, 85 days, 162 days, and 308 days after paving. The positive values in the table indicate tension strains, and a negative value reflects a compressive strain. The performance monitoring of the instrumented pavements lasted for one year after the sensor installation and calibration. Future data collection and evaluation will produce more results for long term evaluation of the pavement health condition.

Table 2. Measured raw and accumulated temperature (environmental) compensated strains.

cell no.	sensor no.	raw strain , με					accumulated strain after temperature compensation, με			
		21 day	52 day	85 day	162 day	308 day	52 day	85 day	162 day	308 day
140	1D-1	-14	38	29	-532	-497	125	134	45	-93
240	1D-2	237	204	122	-655	-516	9.6	-55	-352	-388
140	1D-3	-1251	-956	-927	934	-186	504	413	2746	1463
240	1D-4	106	73	29	-825	-410	-24	10	-364	-218
240	1D-5	-197	-211	-179	-350	15	45	108	415	-614
140	3D-1-L	327	291	209	-414	-219	66	23	-267	-190
140	3D-1-T	272	267	246	-451	-278	100	73	-153	-142
240	3D-2-L	348	420	447	-303	-34	151	181	-90	-5.5
240	3D-2-T	388	423	388	-282	-49	127	77	-133	-53

As known from Chapter 2 that Sensor 1D-3 was placed across the joints in the existing pavements and Sensor 1D-1 was placed in longitudinal direction directly above 1D-3 inside the concrete pavement. Comparing the data of Sensor 1D-3 on different days, it can be seen that, the joint in the existing pavements had extensive tension strain (2,746 με) at 162 days. Since the concrete usually can only hold tension strains up to several hundred according to the research by Liners [32], potential further joint opening might be expected beneath the overlay after six months of overlay casting. Further close monitoring is needed to track the development of these

potential further opening of the beneath joints. With the unbonded design, the pavement above the existing joints behaved well with large tension (130 με) in summer and returned to minor tension (45 με) or compression in winter (-93 με). Considering that concrete materials are strong for compression, which can hold compression strains up to 2 or 3 thousand microstrain depending on the mix design of the concrete [32], no micro-cracks were expected inside the concrete overlay during the monitoring period.

Also, Sensor 1D-5 was placed across the existing transverse crack, and Sensor 1D-4 was placed in the longitudinal direction right above 1D-5 inside the pavement. The measured strains of Sensor 1D-5 showed that although the transverse crack inside the existing pavement sealed with -197 με right after the overlay's casting, it reopens a little in summer with a tension strain around 415 με at 162 days. This significant extension also caused the concrete overlay above to be in tension in summer (10 με) and in compression in winter (-316 με) at 162 days, as indicated from strain recorded by Sensor 1D-4. At 308 days, an abnormal large compression strain was recorded on Sensor 1D-5, indicating that the crack turned to be closing. This closing of the crack in existing pavements may be induced by through-cracks in the current or the adjacent concrete panels. A visual inspection was then performed and a large transverse crack was notified on the west side of the panel as shown in Figure 11, mostly induced by the freezing and thawing effect in spring. The sensors successfully detected abnormal events on the concrete pavements. Continuous close monitoring of the further opening of the transverse crack inside the existing pavements and their influence related to reflective cracking in the pavements was recommended.

Figure 11. The occurrence of transverse cracks on adjacent panel of crack sensors (1D-4 & 1D-5).

In addition, Sensor 1D-2 was installed in the transverse direction inside the pavement. As indicated in Table 2, continuous compressive strains from this sensor indicated an acceptable performance of the overlay in the transverse direction. The longitudinal and transverse components of the two 3D GFRP-FBG sensors both showed tension strains in summer and compression strains in winter. A tension strain of 181 με was noticed in 3D-2-L at the 85 days, indicating that careful attention should be paid on the longitudinal direction. Early longitudinal cracks may be developed with continuous simulated traffic after several season changes. In summer, the pavement sections in Cell 240 were noticed to deform more than Cell 140 with a tension strain difference of around 100 με in longitudinal direction. The regular fabric with a quarter inch (6 mm) of thickness induced a significant tension strain (181 με) in longitudinal direction on the overlay in summer, which may potentially bring up micro cracks in the near future and needs continuous close monitoring. In winter, Cell 140 compressed more than Cell 240 in longitudinal direction with the significant temperature changes. In transverse direction, no significant difference was noticed between the Cell 140 and Cell 240. The monitoring results from the 3D fiber optic sensors indicated that the thinner fabric, Fabric #1 with 8 oz. (236.5 ml) about one-eighth inch (3 mm), performed better than the thicker fabric, Fabric #2 with 15 oz.

(443.6 ml) about a quarter inch (6 mm). The test results approved the theory that thinner fabric will cause less deformation for the overlay, which also proved the potential supports effect from the existing pavements to the above concrete pavements although it was unbonded.

3.1.2. Static loading tests

In addition to the continuous evaluation of the performance of the concrete pavements, static loading tests were also performed on August 1st 2013 and April 18th 2014 to detect the early behavior of the pavements and to validate the system's effectiveness. The MnROAD Truck shown in Figure 10 was again used as the loading truck. Eight loading positions were tested using the MnROAD truck as shown in Figure 12a-h. Loading Position 1 placed the right tire of the front axle on top of Sensor 1D-1, Position 2 loaded the same tire on top of Sensor 3D-1, Position 3 located the right tire of the second axle on top of Sensor 3D-1, Position 4 and 5 situated the right tire of the front axle on top of Sensor 1D-2 and 3D-2, Position 6 and 7 placed the right tire of the second and third axle on top of Sensor 3D-2, and Position 8 loaded the right tire of the fourth axle on top of Sensor 3D-2.

Figure 13 shows the measured strains after temperature compensation from the static field loading tests on August 1st 2013. On August 1st 2013, a static loading of 5.8 kips (2.63 t) on the concrete pavement developed a tension strain of around 50 με in the transverse direction, a tension strain of around 40 με in the longitudinal direction, and a compression strain of around -35 με in the vertical direction. All the sensors in the integrated sensing system recovered after the removal of static loading. The static loads did not induce cracks inside the concrete panels with all the tension strains below 100 με, validating the strength of the mix design of the pavement. However, the truck loading induced relatively large tensile strains in the longitudinal and

transverse directions, which increases the possibility of fatigue cracks with long-term truck traffic.

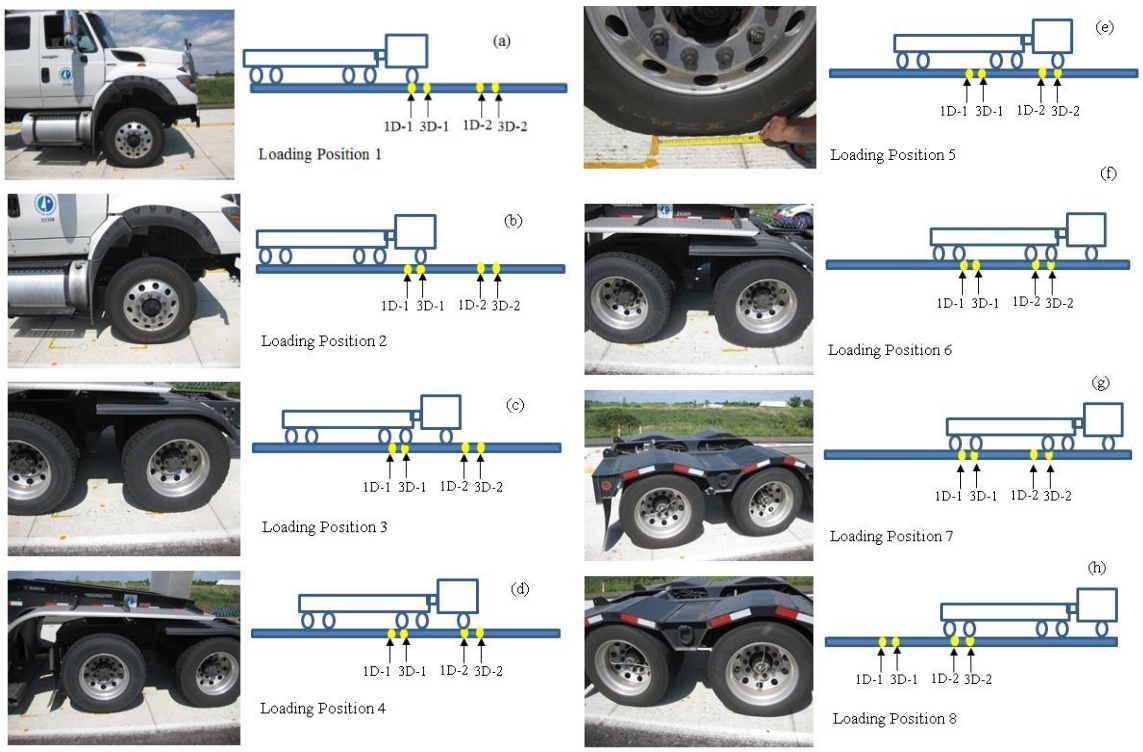

Figure 12. Field static loading testing setup.

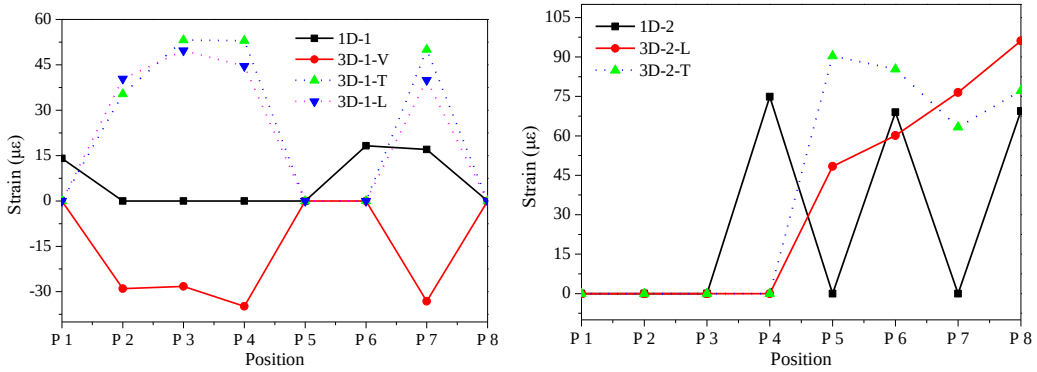

(a) West panel in Cell 140 (b) East panel in Cell 240

Figure 13. Measured temperature compensated strains throughout static testing using the MnROAD semi parked on the sensors of the integrated sensing system on August 1st 2013.

Table 3 shows the comparison of measured strains of the static testing in two different seasons of the integrated sensing system on August 1st 2013 (Season of summer & fall) and April 18th 2014 (Season of winter & spring). It is clearly demonstrated that the concrete pavement and its foundation acted much stiffer in winter season than in summer season with smaller strains in general for all loading cases. The phenomenon of stiffer concrete pavement was also attributed to the continuous dynamic loading with heavy vehicles on the pavements. In the winter season, the strain differences between two fabric types are smaller than in summer season.

Table 3. Comparison of measured strains on August 1st 2013 and April 18th 2014.

Position	Strains on August 1st 2013 (με)					April 18th 2014 (με)				
	3D-1-V	3D-1-T	3D-1-L	3D-2-T	3D-2-L	3D-1-V	3D-1-T	3D-1-L	3D-2-T	3D-2-L
position 2	-29	49	40	0	0	-17	35	18	0	0
position 3	-30	53	48	0	0	-20	42	26	0	0
Position 5	0	0	0	90	60	0	0	0	62	33
Position 6	0	0	0	85	76	0	0	0	51	45

3.2. Road Roughness Evaluation[1]

Road roughness is another parameter which assists pavement maintenance resource allocations. Traditionally, the road roughness evaluation is performed using road profiler instrumented on automobiles as mentioned in Chapter 1. Enabling the capability of road roughness measurements using the integrated sensing system with in-pavement strain sensors

[1] © IOP Publishing. Reproduced with permission. All rights reserved
http://iopscience.iop.org/article/10.1088/0964-1726/24/11/115029/pdf

will impact significantly the road management system for cost-effective maintenance resource allocation. This section, thus, develops a methodology to use the developed integrated sensing system for road roughness evaluation through systematic theoretical, numerical, and experimental analysis.

3.2.1. Theoretical analysis

Roughness occasionally exists as part of the roadway design or construction defects [73], and pavement wear increases the roughness levels over time since a deformation of the pavement structure would produce a change in the road profile. Consequently, a deformation-induced increase of strain within the pavement structure must correspond to an accumulation of profile unevenness. This study uses concrete pavements for the theoretical analysis. According to the Kirchhoff–Love plate theory [74], the strain in the longitudinal (x) direction of a thin-plate concrete panel, ε_x, located inside the pavement at some known vertical position h_0, is expressed as:

$$\varepsilon_x = -h_0 \frac{d^2 w}{dx^2}, \tag{4}$$

where w is the vertical displacement of the concrete pavement panel which is also known as the road elevation profile. With the sampling interval requirement satisfied, double integration of Equation (5) reproduces the relation between the road elevation profile and the measured strains from the in-pavement sensors as:

$$w = -\iint \frac{\varepsilon_x}{h_0} dx. \tag{5}$$

The IRI then becomes available because the slope rate of the road profile, $\ddot{w}$, which is the second derivative of the elevation profile, w, with respect to time, is a direct input to the

procedure that computes the IRI. For a temporal road profile of ξ, the second derivative with respect to time is

$$\ddot{\xi} = -\ddot{w} = \frac{v^2 \varepsilon_x}{h_0} \tag{6}$$

where v = 80 km/h is the IRI standard speed [33].

The Highway Safety Research Institute (HSRI) defines the IRI in terms of the responses from a standard quarter-car model having two degrees of freedom as shown in Figure 14.

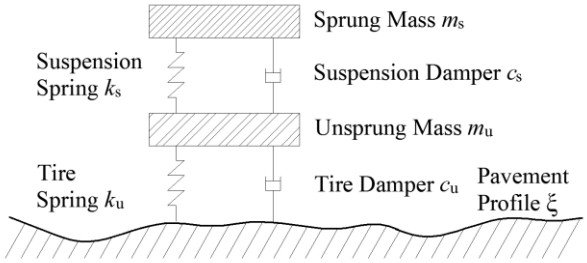

Figure 14. The HSRI quarter-car model.

The parameters y^t_s and y^t_u are absolute displacements of the sprung- and unsprung-mass, respectively. The HSRI quarter-car parameters are k_u/m_s = 653.0 s^{-2}, k_s/m_s = 63.3 s^{-2}, m_u/m_s = 0.15, c_s/m_s = 6.0 s^{-1} and c_u/m_s = 0.0 s^{-1}. Let the relative displacement of sprung mass be y_s and that of the unsprung mass be y_u such that

$$y_s = y^t_s - y^t_u \qquad \text{and} \qquad y_u = y^t_u - \xi. \tag{7}$$

Expressed in matrix-form, the ordinary differential equations to define the system dynamics for the sprung and unsprung mass is

$$M\ddot{Y}(t) + C\dot{Y}(t) + KY(t) = R(t) \tag{8}$$

where

$$M = \begin{bmatrix} m_s & m_s \\ 0 & m_u \end{bmatrix}, C = \begin{bmatrix} c_s & 0 \\ -c_s & c_u \end{bmatrix}, K = \begin{bmatrix} k_s & 0 \\ -k_s & k_u \end{bmatrix},$$

$$\ddot{Y} = \begin{Bmatrix} \ddot{y}_s \\ \ddot{y}_u \end{Bmatrix}, \dot{Y} = \begin{Bmatrix} \dot{y}_s \\ \dot{y}_u \end{Bmatrix}, Y = \begin{Bmatrix} y_s \\ y_u \end{Bmatrix}, \text{and } R = \begin{Bmatrix} -m_s \ddot{\xi} \\ -m_u \ddot{\xi} \end{Bmatrix} \tag{9}$$

Substituting Equation (6) into Equation (9) provides the expression:

$$R = \begin{Bmatrix} -m_s \dfrac{v^2 \varepsilon_x}{h_0} \\ -m_u \dfrac{v^2 \varepsilon_x}{h_0} \end{Bmatrix} \tag{10}$$

Solving Equation (8) with a numerical algorithm such as the Newmark method yields the relative displacements y_s and y_u, the relative velocities $\dot{y}_s$ and $\dot{y}_u$, and the relative accelerations $\ddot{y}_s$ and $\ddot{y}_u$ as a function of the in-pavement strains and velocities of the vehicle. The IRI is then [33]:

$$\text{IRI} = \frac{1}{L} \int_0^T |\dot{y}_s| \mathrm{d}t \tag{11}$$

in which, L is the segment length and $T = L/v$ is the travel time. For a computational sample interval of Δt, the number of intervals is $n = T/\Delta t$ and the discrete-time form of the computation becomes

$$\text{IRI} = \frac{1}{vn\Delta t} \sum_{i=0}^{n} |\dot{y}_s(t_i)| \Delta t = \frac{1}{vn} \sum_{i=0}^{n} |\dot{y}_s(t_i)|. \tag{12}$$

3.2.2. Sensitivity study

This section conducts the sensitivity study of the roughness evaluation process displayed in Section 3.2.1. The factors influencing the accuracy of the IRI estimation using the measurements from in-pavement strain sensors mainly include the implementation sensor interval and the sensor signal's quality characterized by the signal-to-noise ratio (SNR). From

Equation (6), it can be seen that the in-pavement strain is directly proportional to the second derivative of the profile ($\ddot{\xi}$). The interval of the road profile samples (ξ) and the second derivative of the profile ($\ddot{\xi}$) can represent the strain sensor position intervals and the output signal of the sensors, respectively.

To simulate road profiles (ξ) of different roughness levels for sensitivity analysis, the inverse fast Fourier transform (IFFT) of the PSD is a suitable approach to apply [75, 76]. For this analysis, the second-order forward difference provides a higher-accuracy numerical approximation of the second derivative of the profile ($\ddot{\xi}$) [77]. After solving Equation (8) using the Newmark method, Equation (12) then provides the associated IRI for the profile [77]. The variation in IRI is observable by changing the profile sampling interval size, which represents the strain sensor interval, for each evaluation of Equation (8). The method of noise sensitivity analysis involves adding white Gaussian noise to the in-pavement strains (ε_x) thus, to the profile's slope rate ($\ddot{\xi}$), and observing the IRI variations.

3.2.2.1. Roughness generation

The ISO (1995) [78] represents the elevation profile (ξ) as a PSD such that

$$S_\xi(\kappa) = \begin{cases} S_\xi(\kappa_0)\left(\frac{\kappa}{\kappa_0}\right)^{-n_1} & \frac{\kappa}{\kappa_0} \le 1 \\ S_\xi(\kappa_0)\left(\frac{\kappa}{\kappa_0}\right)^{-n_2} & \frac{\kappa}{\kappa_0} > 1, \end{cases} \tag{13}$$

where, κ is the wavenumber with a unit of cycle/m, κ_0 is the datum wavenumber in cycle/m, $S_\xi(\kappa)$ is the road profile PSD in an unit of m^3/cycle, and $S_\xi(\kappa_0)$ is the PSD at κ_0 or initial PSD in m^3/cycle.

For typical profiles, Cebon [79] recommended n_1=3, n_2=2.25, and κ_0=1/(2π) cycles/m. Table 4 summarizes the qualitative relationship between the roughness classification and the initial PSD. As expected, higher values of $S_\xi(\kappa_0)$ corresponds to poorer road condition in terms of roughness levels.

Table 4. Relationship between roughness classification and initial PSD [79].

Roughness Classification	$S_\xi(\kappa_0)$ 10^{-6} m^3/cycle
Very Good	2-8
Good	8-32
Average	32-128
Poor	128-512
Very Poor	512-2048

Reference [80] indicates that the IRI does not respond to spatial wavelength components that fall outside of the 1.3 m to 30 m wavelength band. Therefore, the κ range from 0.02 cycle/m to 5 cycle/m is conservative for the IFFT computation. Figure 15a shows the road profile generated with $S_\xi(\kappa_0) = 3.2\times10^{-5}$ m^3/cycle, and Figure 15b shows the corresponding PSD.

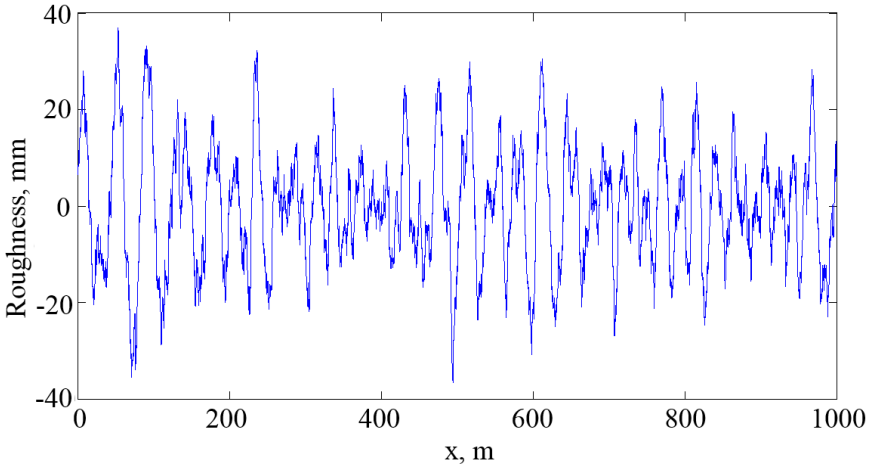

(a) Generated Road Profile

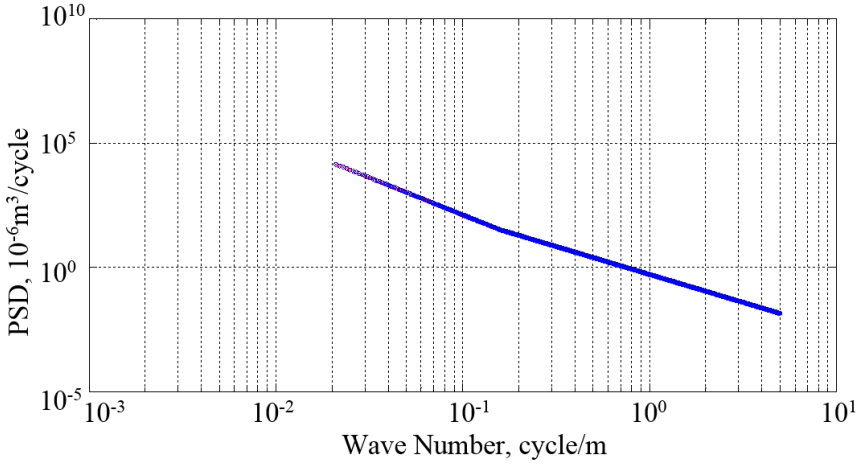

(b) Comparison on the Power Spectral Density

Figure 15. Roughness generation at $S_\xi(\kappa_0) = 3.2\times10^{-5}$ m^3/cycle.

3.2.2.2. Sensitivity on in-pavement strain sensor interval

The sensor interval is defined as the distance between sensors installed inside the pavements along the road sections in this dissertation. It is an important factor for the signal quality, as it is a direct indicator of resolution for the roughness data collection. The Nyquist-Shannon sampling theorem dictates a minimum profile sampling interval of 0.65 m because the IRI becomes insensitive to wavelengths shorter than 1.3 m. Figure 16 shows the change of IRI with the sensor interval for the roughness generated at $S_\xi(\kappa_0) = 3.2\times10^{-5}$ m^3/cycle. As shown in Figure 16, the IRI steadily decreases as sensor interval increases. The tradeoff between IRI

accuracy and in-pavement strain sensor interval directly relates to the expense of sensor installation. The recommended standard sampling interval is 0.3 meters using the vehicle based profiling approaches [8]. However, installing strain sensors at the equivalent sampling intervals would require a significantly large number of strain sensors that would result in a high initial installation cost.

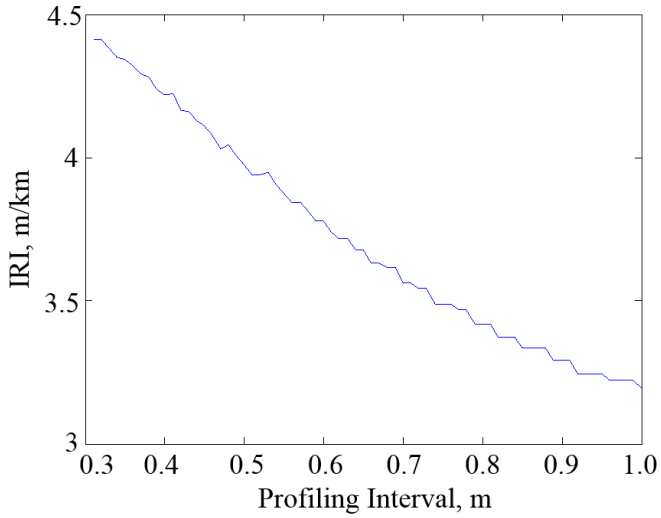

Figure 16. IRI at different strain sensor intervals.

To potentially reduce the number of sensors needed for a more cost-effective solution, Table 5 compares various sensor interval compared with the IRI calculated from standard intervals of 0.3 m for different levels of roughness $S_\xi(\kappa_0)$ with measurement accuracies of 90% and 80%. The results indicate that larger IRI or rougher surfaces require fewer sensors. Since the road roughness matter more when the IRI increases, users can increase the sensor interval to decrease cost without losing measurement accuracy. A sensor interval of 0.7~0.8 m would provide an accuracy within 80% for roughness levels that correspond to the road conditions with average or below that matter most to the agencies. Hence, trading off 20% accuracy reduces the

required number of in-pavement strain sensors by at least a factor of two. For specific applications, a sensor interval analysis is highly recommended before the sensor installation.

Table 5. Sensor intervals required for an accuracy of 80% and 90%.

$S_\xi(\kappa_0)$, 10^{-6} m^3/cycle	2	4	8	16	32	64	128	256	512	1024	2048
IRI at 0.3 m, m/km	1.12	1.57	2.23	3.19	4.55	6.33	8.92	12.76	17.95	25.04	36.14
Sensor Interval with 90% Accuracy, m	0.3	0.3	0.3	0.4	0.4	0.5	0.5	0.5	0.5	0.5	0.5
Sensor Interval with 80% Accuracy, m	0.4	0.5	0.6	0.6	0.7	0.7	0.8	0.7	0.7	0.8	0.8

3.2.2.3. Sensitivity on sensor signal quality

This section uses the ASTM Standard E 1926-98 [33] profile with known IRI to study the noise sensitivity of the in-pavement strain sensor on IRI estimation. Figure 17 shows the simulated standard sinusoidal road profile. Table 6 lists the calculated IRI values and the relative errors for different levels of white Gaussian noise. The relatively small error of 5.0% between the IRI of the ASTM profile and the IRI computed from generating the slope rate estimated from the strain-based method in this study validates the method. Adding noise levels ranging from 3 dB to 10 dB to the slope rate of the profile estimated from the strain-based approach result in relative errors that are less than 5% as listed. This result demonstrates that the developed strain-based roughness estimation method is relatively insensitive to noise.

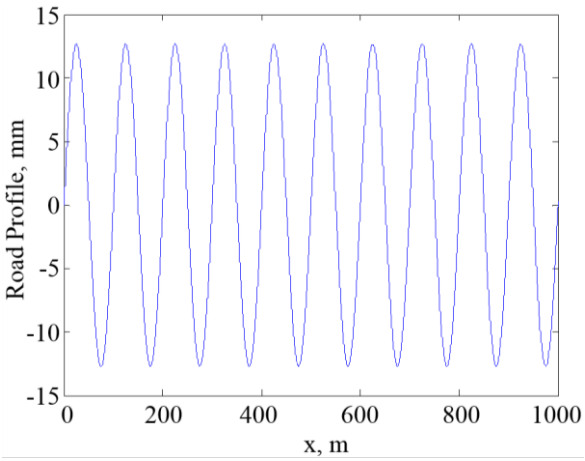

Figure 17. Road profile (ASTM Standard E 1926-98 [33]).

Table 6. Validation of the method for IRI calculation.

Parameter	ASTM	Strain-based Method from This Study			
		No Noise	3 dB Noise	8 dB Noise	10 dB Noise
IRI	0.0222	0.0211	0.0226	0.0216	0.0215
Relative Error	-	5.0%	1.8%	2.7%	3.2%

3.2.3. Field experimental validations and discussions

The high-resolution localization feature of the connected-vehicle method of roughness characterization provided validation for the in-pavement strain sensor method. The Cell-40 at MnROAD introduced in Chapter 2 with integrated sensing system instrumented was applied to validate the derived roughness index in this Chapter. Figure 18a shows the seventy concrete pavement panels of Cell 40 for roughness evaluation; they are numbered Panel 0 through Panel 69. The length of each panel is 6 ft, so the total length of test section is 420 ft. Figure 18b is a photo of the concrete panel series in Cell-40 for visual evaluation. The sensor layout of the integrated sensing system is referred back to Figure 8 in Chapter 2.

(a) Plane view of the testing panels (b) Photo of Cell-40

Figure 18. Road sections at MnROAD for roughness evaluation.

As shown in Figure 16, the analysis treats the strain distribution along the wheel path of each panel as step functions. Following the procedure mentioned above for the strain-based method, the estimated IRI values for the three panels with instrumented in-pavement GFRP-FBG sensors are 3.33, 3.34, and 3.19 for Panel 36, Panel 40, and Panel 53, respectively.

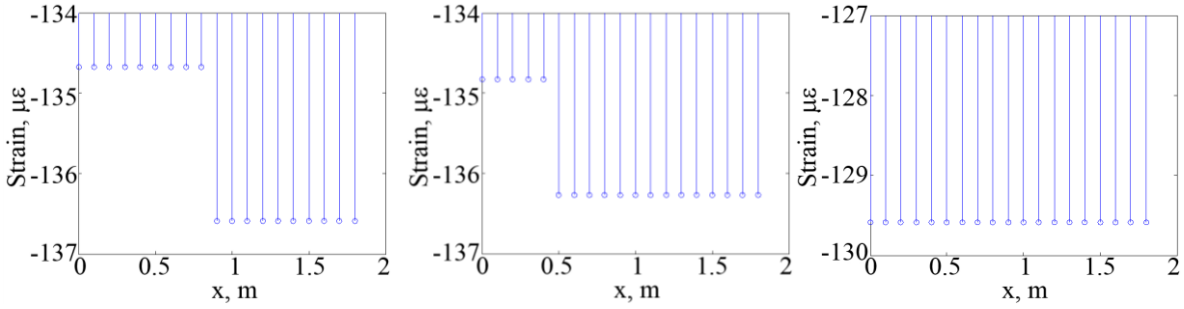

(a) Panel 36 (b) Panel 40 (c) Panel 53

Figure 19. Strain distribution along the wheel path track of each testing panel.

This study used a regular passenger vehicle, a 2011 Chevrolet Traverse as shown in Figure 20, to collect the inertial and geospatial position data needed for the RIF-transform [81]. Three smart phones with a data logger application (app) were secured flat in the vehicle's rear trunk and logged the resultant vertical accelerations. Figure 21 shows a top view of the smartphone installation, including their orientations. Phone 1 and Phone 2 were iPhone® 4S

devices fixed in the longitudinal orientation whereas Phone 3 was an iPhone® 5 oriented in the lateral direction. The GPS receiver had an update rate of 1 Hz and the accelerometer was set to sample at 128 Hz based on recommendations from prior studies [82]. The iOS® app logged inertial and geospatial position data as the vehicle traversed the 70 panels selected for roughness evaluation.

Figure 20. Passenger vehicle for roughness evaluation (2011 Chevrolet Traverse).

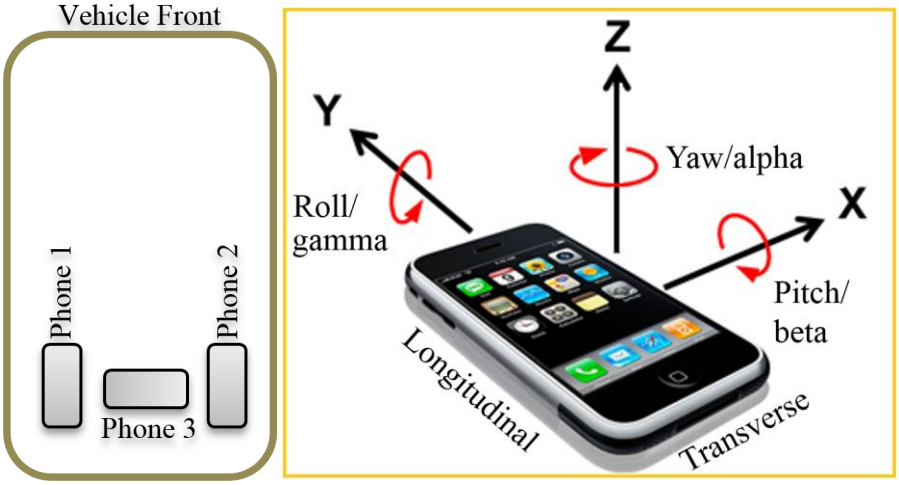

(a) Smart Phone Layout (b) Orientation of Smart Phone

Figure 21. Smart phone installation at the rear trunk for fielding testing.
[Note: Phone size and appearance for demonstration only and not for the real field testing, for real tests on site, please refer to the available smart phones on site.]

The EAR-index for the three panels deployed with the in-pavement GFRP-FBG strain sensors are 0.149, 0.162, and 0.144 for Panel 36, Panel 40, and Panel 53, respectively.

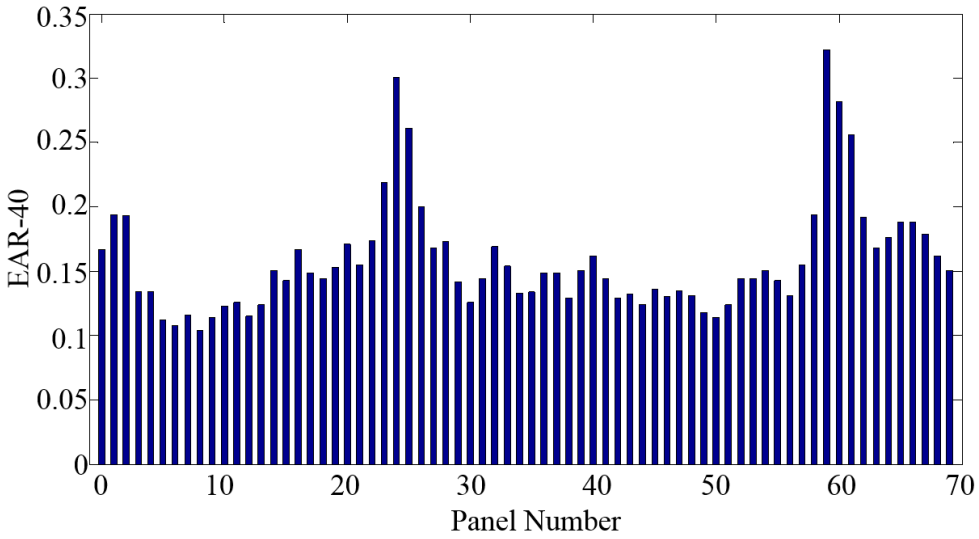

Figure 22. Estimated EAR-index for Panel 0-69 using connected vehicle method.

The direct proportionality relationship between the IRI and the EAR-index provides a cost-effective means of validating the developed roughness estimation method using in-pavement strain sensors by comparing it with the respective roughness indices obtained from the connected vehicle approach for the three panels. Table 7 compares the estimated IRI using the strain-based method and the obtained EAR-indices from the connected-vehicle method for Panel 36, Panel 40, and Panel 53 and their ratios. The ratios of the IRI to the EAR-indices for the three panels range from approximately 20 to 23. The estimated IRI is proportional to the EAR-indices at an average ratio of 21.71, and the standard deviation of the ratios is only 3.6% of the mean. This indicates a high degree of consistency in the IRI values derived from the developed strain-based method. It demonstrates that the IRI estimated from the in-pavement strain sensors is directly proportional to the EAR-indices from the connected-vehicle method as expected, and this result validates the effectiveness of the IRI evaluation using the in-pavement strain sensors.

The accuracy of roughness evaluation was further validated with IRI values measured from profiling measurements of the same road section by a transportation management agency [83].

Table 7. Comparison of IRI and EAR-index on sensor-deployed panels.

	Panel 36	Panel 40	Panel 53
IRI derived from strain-based method	3.33	3.34	3.19
EAR-index from the connected-vehicle method	0.149	0.162	0.144
IRI/EAR-index	22.35	20.62	22.15

3.3. Summary

This study provides transportation researchers and engineers with a cost-effective method of road condition assessment and roughness evaluation using the integrated sensing system deployed inside the pavement. The conclusions of this section are as follows:

1) Field studies approve that the integrated sensing system is capable to detect the early performance of the instrumented pavements for road condition assessments;
2) The strains obtained from the integrated system can be used to derive the roughness of the instrumented road section theoretically for road roughness evaluation;
2) Numerical simulation proves that the integrated sensing system is able to measure the road roughness with a measurement accuracy of 80% or higher at a specific sensor implementation interval of 0.7 m or shorter for the roughness levels that are of most concern to agencies and this approach is relatively insensitive to the noise disturbances.
3) The case studies validated the new roughness evaluation method based on the integrated sensing system by comparing the consistency of its proportionality with a connected-vehicle method of roughness characterization that is directly proportional to the IRI.

The results of this research provide an alternative method of road condition assessment and roughness evaluation that does not require probe vehicles. This new method will provide roadway agencies with the ability to evaluate road condition and roughness in real time and continuously throughout the service life of the road to enable improved methods of predictive asset management, and the potential for significant lifetime cost savings.

4. WEIGH-IN-MOTION MEASUREMENTS[2]

Weights of the passing vehicle are very critical information for traffic management and enforcements. The advances of WIM technology makes it possible to achieve high-speed WIM measurements. In this chapter, the developed integrated sensing system was applied for high-speed WIM measurements. The detail theoretic derivations of the relations between the measured strains in the pavements to that of the WIM on road are delivered with numerical sensitivity study and field experimental validations.

4.1. General Theoretical Analysis

The rolling weight of the wheel contact area across the in-pavement strain sensors of the integrated sensing system produces the strain signal when the vehicle traverses the instrumented pavement sections. The quality of the strain signal directly affects the accuracy of the measurement. The appropriate sampling rate and signal-to-noise ratio will minimize strain signal distortions and maximize the measurement accuracy to distinguish the weight profile of different vehicles passing at the maximum design speed. The strain signal obtained from the integrated system is a convolution of the load from the wheel contact area and the sensitivity function of the in-pavement sensors. A Fourier transform of the resulting strain signal and the Nyquist-Shannon sampling theorem provide the theoretical foundation for selecting the minimum sampling rate.

Theoretically, when one vehicle tire traverses the top of the in-pavement sensors of the integrated sensing system and the distance between two axles is sufficiently long to distinguish the signal from adjacent tire crossings, the sensors' strain signal becomes the convolution of the pressure distribution from the vehicle's tire contact area and the sensitivity function of the in-

pavement sensor. For a specific tire, if the contact pressure $p(x, y)$ at a location (x, y) inside the contact area has a length of L_0 and a width of B_0 (Figure 23a) then the compressive force P of the whole tire is

$$P = \int_{L_0 \times B_0} p(x, y)\mathrm{d}s \,. \tag{14}$$

Integrating the contact pressure $p(x, y)$ in the lateral dimension (y direction) aligns the pressure function with the longitudinal sensitivity of the sensor, P_{L}, as:

$$P_{\mathrm{L}} = \int_{-B_0/2}^{B_0/2} p(x, y)\mathrm{d}y. \tag{15}$$

Assume that the longitudinally deployed strain sensor has a sensitivity function of S_{L} along the length of the sensor. The sensitivity is a function of sensor resolution, installation depth, and properties of pavement. Figures 23b and 23c illustrate area-equivalent functions of the compressive force $P_{\mathrm{L}}(t)$ and the sensor's sensitivity $S_{\mathrm{L}}(t)$ respectively during the traversal period.

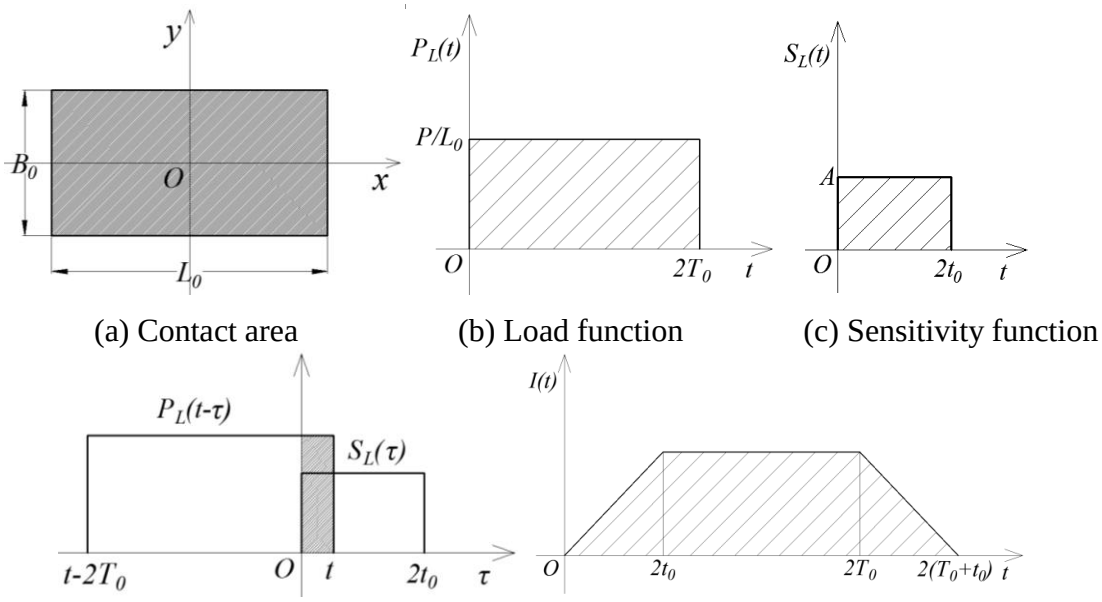

(a) Contact area (b) Load function (c) Sensitivity function

(d) Convolution (e) Strain signal

Figure 23. Operation to acquire the strain signal in pavements by convolution.

Their respective durations $2T_0$ and $2t_0$ result from traversals at some specified speed. Therefore, the strain signal, $I(t)$, is a convolution of $P_L(t)$ and $S_L(t)$ as illustrated graphically in Figures 23d and 23e:

$$I(t) = \int_{-\infty}^{+\infty} P_L(t-\tau) S_L(\tau) v \mathrm{d}\tau \tag{16}$$

such that $I(t)$ is zero outside the interval $[0, 2(T_0+t_0)]$.

The Fourier transform of the strain function in Equation (16) provides the frequency distribution to guide the selection of the optimum sampling rate. Given a finite strain signal, $I(t)$, in isolation, the Fourier transform [84] is:

$$I(\omega) = \int_{-\infty}^{+\infty} I(t) \exp(-i\omega t) \mathrm{d}t. \tag{17}$$

The convolution property of Fourier transform [84] dictates that a convolution in the time domain is equivalent to a multiplication of the frequency domain functions. Thus, the Fourier spectrum of $I(t)$ is:

$$I(\omega) = v P_L(\omega) S_L(\omega). \tag{18}$$

where $P_L(\omega)$ and $S_L(\omega)$ are the Fourier transforms of the load function $P_L(t)$ and the sensitivity function $S_L(t)$, respectively.

The Nyquist-Shannon sampling theorem [85] posits that the minimum sampling rate required to capture the signal energy is twice the strain signal bandwidth B_ω such that:

$$F_S = 2B_\omega. \tag{19}$$

Therefore, deriving the strain signal theoretically will guide the sampling rate requirement for high-speed WIM measurements using the integrated sensing system with in-pavement strain-based sensors.

4.2. Theoretic Analysis of the Case Study

The case study discribed in Chapter 2 with the integrated sensing system instrumented in concrete pavements was used to validate the general theories of the previous section.

The area-equivalent tire pressure along the wheel path is a constant value within the contact area ($L_0 \times B_0$) such that when travelling at a speed (v), the pressure function, $P_L(t)$, from Equation (15) becomes:

$$P_L(t) = \frac{P}{L_0} \Pi\left(\frac{t - T_0}{2T_0}\right) \tag{20}$$

The time-shift of $T_0 = \frac{L_0}{2v}$ produces a causal signal. The rectangular function $\Pi(t)$ is:

$$\Pi(t) = \begin{cases} 0 & if \quad |t| > \frac{1}{2} \\ \frac{1}{2} & if \quad |t| = \frac{1}{2} \\ 1 & if \quad |t| < \frac{1}{2} \end{cases}. \tag{21}$$

The aspect ratio, defined as the minimum of length and width divided by thickness, is typically between 8 and 80 for the slab of a concrete pavement. The mechanistic model is a rectangular thin plate supported by an elastic foundation. The mechnical behavior of thin plates supported by upward springs (elastic foundation) exhibited no significant differences with different boundary conditions [86]. The Kirchhoff plate theory [87] yields the maximum of strain sensitivity function as

$$A = \frac{4\pi^2(1-\eta)(h/2 - h_0)}{a^3 b} \sum_{m=1}^{\infty} \sum_{n=1}^{\infty} \frac{m^2}{\pi^4 D\left(\frac{m^2}{a^2} + \frac{n^2}{b^2}\right)^2 + k} \sin^2 \frac{m\pi x_0}{a} \sin \frac{n\pi y_0}{b} \sin \frac{n\pi q_0}{b}, \tag{22}$$

where 1-η is the strain transfer coefficient, h is the thickness of pavement panel, h_0 is the depth of sensor in the pavement, a and b are the length and width of pavement panel respectively, D is

the flexural rigidity of plates, k is the stiffness of the elastic foundation, x_0 and y_0 are the position of sensor location, and q_0 is the transverse location of the wheel path. The flexural rigidity D is:

$$D = \frac{Eh^3}{12(1-\mu^2)}, \tag{23}$$

where E, h, and μ are the moduli of elasticity, the thickness, and the Poisson ratio of the plate, respectively.

The area-equivalent rectangular function [16] has a constant intensity of A and a length of L_S as shown in Figure 24. Therefore, the sensitivity function $S_L(x)$ in the time domain is:

$$S_L(t) = A\Pi\left(\frac{t-t_0}{2t_0}\right) \tag{24}$$

where $t_0 = \frac{L_S}{2v}$ and the equivalent length, L_S, is:

$$L_S = \frac{\int_0^a S_L(x)dx}{A} \tag{25}$$

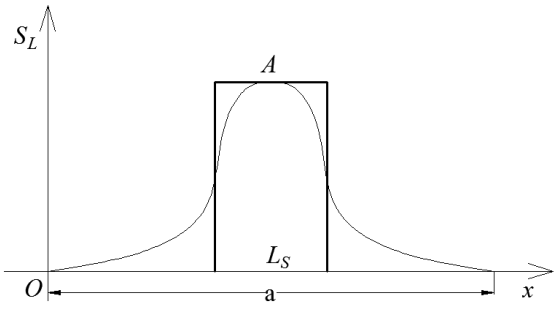

Figure 24. Strain sensor's sensitivity function and the equivalent rectangular function.

Using Fourier transform, the spectra of the load and sensitivity function, respectively, are

$$P_L(\omega) = \frac{P}{v}\exp(-i\omega T_0)\,\mathrm{sinc}\,(\omega T_0/\pi) \text{ and } S_L(\omega) = 2At_0\exp(-i\omega t_0)\,\mathrm{sinc}\,(\omega t_0/\pi) \tag{26}$$

where, $\mathrm{sinc}(x) = \sin(\pi x)/\pi x$. The frequency domain equivalent of their convolution is:

$$I(\omega) = \frac{AL_S P}{v^2} \exp[-i\omega(t_0 + T_0)] \operatorname{sinc}(\omega t_0 / \pi) \operatorname{sinc}(\omega T_0 / \pi) \tag{27}$$

Figure 25 shows the magnitude as a function of frequency. As observed, most of the strain signal's energy is concentrated within the first lobe, termed as main lobe. The width of the main lobe was defined as its fundamental bandwidth [88]. Therefore, the fundamental bandwidth of the strain signal is:

$$B_\omega = \frac{\pi}{T_0}. \tag{28}$$

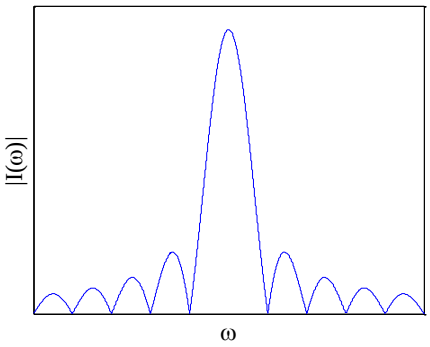

Figure 25. Illustration of the magnitude of $I(\omega)$.

Thus, in theory, the minimum sampling rate required to capture the fundamental energy of the strain signal is:

$$F_S = \frac{2B_\omega}{2\pi} = \frac{1}{T_0}. \tag{29}$$

where, the determination of B_ω is dependent on the comparison between T_0 and t_0 for the relative dominance of the energy within the main lobe of $I(\omega)$.

4.3. Numerical Analysis

This section conducts numerical simulations using the theories presented above using the in-pavement strain gauge of the integrated sensing system as shown in Figure 8(a), shown again

in Figure 26 for the dimensions of the concrete pavement segment and the sensor layout that creates the high-speed strain gauge of the integrated system installed at the MnROAD facility [89]. The strain gauge is in the wheel path and orients in the longitudinal direction. The numerical analysis applies a load of 5,800 pounds (P) to simulate the weight of the front right tire of a five-axle MnROAD truck [18] with a tire contact area of 13.8 in. (L_0) × 9 in. (B_0). The truck wheel path is located 42.5 in. (q_0) away from the edge of the pavement panel. The truck moves at a constant speed of 39 mph (v). Table 8 summarizes the parameters used to evaluate Equation 22. Based on the case study introduced in Chapter 2 and 3, the size of the test pavement panel is 72 in. of length (a) and width (b) and 3 in. of thickness (h). The sensor is installed 52.1 in. (x_0) and 45.2 in. (y_0) away from the edge of the panel and at a depth of 2.8 in. (h_0). The length of the sensor can be considered as 1.4 in. (L_S). In Table 8, it is also worth noticing that the elastic modulus of the concrete was tested to be around 2,176 ksi (E) with a passion ratio of 0.16 (μ), which are provided by MnROAD engineers. Figures 27a and 27b shows the resulting strain signal and the magnitude of its Fourier transform respectively. The rectangular function equivalents used for the load and sensitivity functions produce the trapezoidal shape of the strain signal and the sinc function of its spectra as theorized. The expected amplitude and bandwidth of the strain signal is 77.57 με and 312.52 rad/sec respectively. The sampling rate (F_S) based on the fundamental bandwidth is 100 Hz.

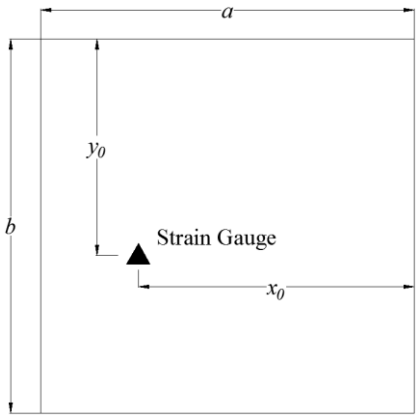

Figure 26. Strain gauge configuration in the concrete pavement.

Table 8. Parameters for numerical simulation.

Parameter	Value	Unit	Parameter	Value	Unit
a	72	in.	E	2,175,566	psi
b	72	in.	k	1078	pci
P	5,800	lb	h_0	2.8	in.
L_0	13.8	in.	η	0.01	-
B_0	9	in.	x_0	52.1	in.
v	39	mph	y_0	42.5	in.
μ	0.16	-	q_0	42.5	in.
h	3	in.	L_S	1.69	in.

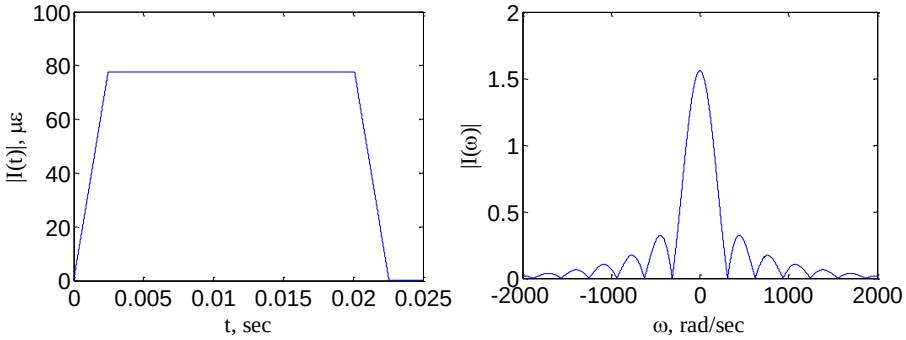

(a) $I(t)$ (b) $I(\omega)$

Figure 27. Strain signal $I(t)$ and its Fourier spectrum

Figures 28a and 28b show the strain signal in the time and frequency domains respectively after sampling at 100 Hz. As expected, the exclusion of harmonics beyond the fundamental frequency results in a loss of signal energy that creates the sharp transitions. Its peak intensity of 91.07 με is 17% larger than that of the ideal signal.

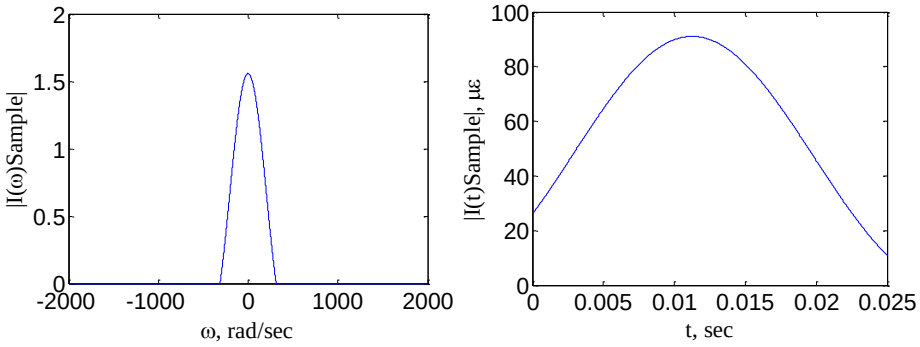

(a) Fourier spectrum (b) Time domain signal

Figure 28. Simulated strain signal at a sampling rate of 100 Hz

The peak intensity approaches the ideal signal magnitude asymptotically as sampling rate increases. Figure 29 shows the strain signal from sampling at rates of 2, 8, and 32 times greater, or equivalently at 200 Hz, 800 Hz, and 3.2 kHz. The strain signal magnitudes are 86.07 με, 78.4 με, and 77.88 με, respectively. Hence, the errors are 10%, 1%, and 0.4%, respectively. On the other hand, the data storage requirements increase proportionally. For example, using 6 bits per sample will result in a daily storage requirement per sensor of 6.48 MB, 12.96 MB, 51.84 MB, and 207.36 MB, corresponding to the 100 Hz, 200 Hz, 800 Hz, and 3.2 kHz sampling rates [90]. In most cases, the high-speed WIM system will use 4 strain sensors to measure the weight of entire vehicles. For such a scenario, the daily storage space requirement to achieve measurement accuracies of 89.04%, 98.93%, and 99.6% will be 51.84 MB, 207.36 MB, and 829.44 GB respectively. Consequently, the trade-off in storage space and accuracy is a significant consideration in the design of high-speed WIM systems.

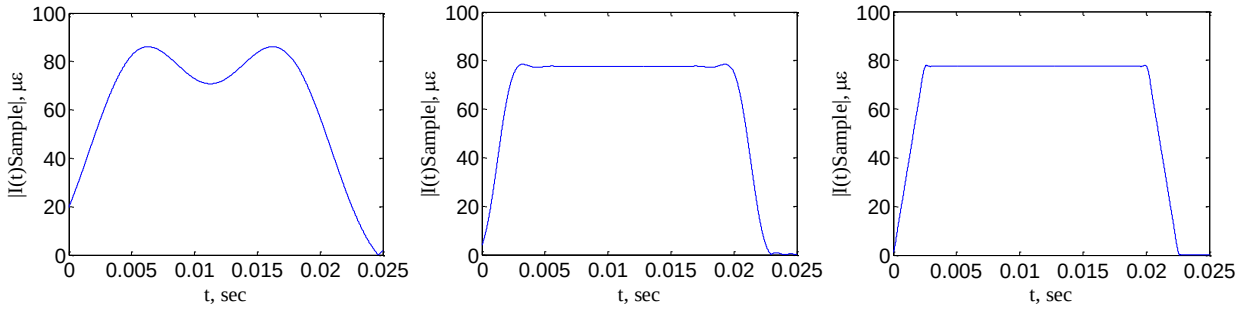

(a) 200 Hz (b) 800 Hz (c) 3.2 kHz

Figure 29. Signal sampled at different rates.

Table 9 shows the sampling rates needed to capture the fundamental frequency of strain signals resulting from traversals of 5 mph to 100 mph. It is evident that the sampling rate increases almost linearly as a function of vehicle speed. Hence, if an accuracy of 85% is acceptable for high-speed WIM measurements, then a sampling frequency of 255 Hz should accommodate traversal speeds up to 100 mph for the case study.

Table 9. Sampling rates for different speeds.

v, mph	5	10	20	30	40	50	60	70	80	90	100
F_S, Hz	13	26	51	77	102	128	153	179	204	230	255

4.4. Field Validations and Discussion

The integrated sensing system implemented at the MnROAD facility mirrors the arrangement of the theoretical development and the numerical analysis as in Section 4.3 [89]. Figure 30 shows the MnROAD truck used to traverse the sensor at 39 mph. Sampling the strain gauge at 1.2 kHz provides a sufficiently high rate to examine the effects of sampling rate reduction by post filtering. Figure 31 shows the strain signal acquired from the strain gauge in the unit of με. The five pulses coincide with the five axle traversals of the MnROAD truck.

Figure 30. Field tests at MnROAD facility.

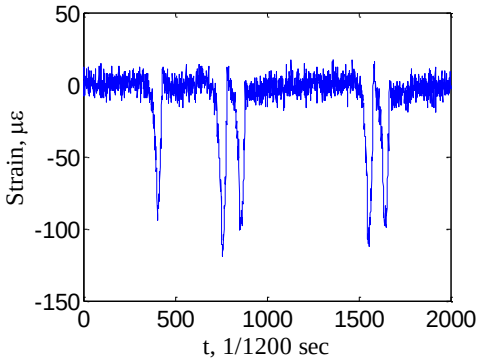

Figure 31. Measured signal from the strain gauge at 1.2 kHz.

Preliminary analysis indicated that a 7th order Bessel filter would provide a suitable tradeoff in noise reduction and signal distortion from passband phase response [91]. Figure 32 shows the magnitude and phase response of the 7th order Bessel filter with cutoff frequency f_c = 75Hz. Figure 33a provides a detailed view of the first pulse in Figure 31. It corresponds to the first axle crossing the sensor. Isolating the first pulse maintains consistency with the numerical simulation in Section 4. Figure 33b shows the filtered strain signal. It is evident from the comparison between Figure 33a and Figure 33b that the digital filtering minimized the noise and adequately preserved the magnitude of the strain signal.

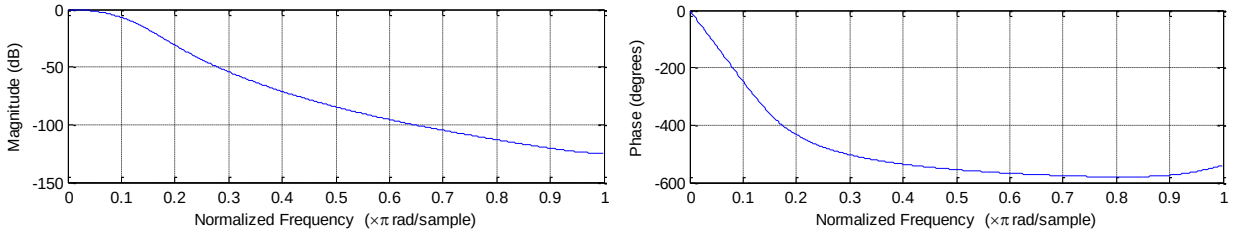

(a) Magnitude (b) Phase

Figure 32. The 7th order digital Bessel filter

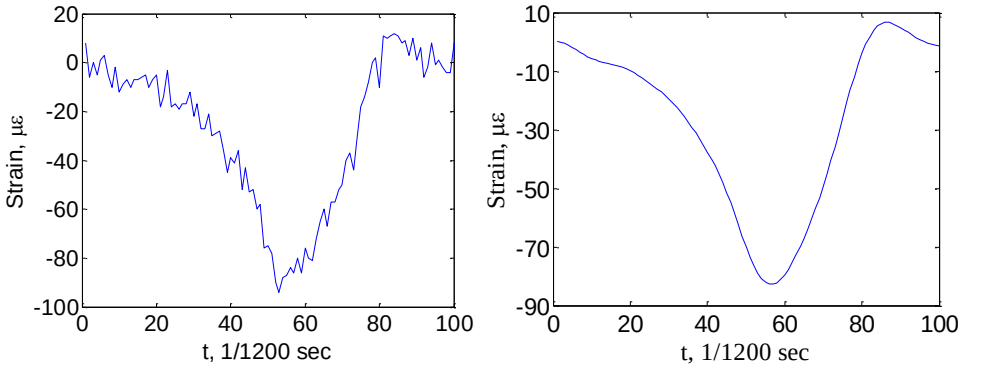

(a) Measured signal (b) Digital filtered signal at f_c = 75 Hz

Figure 33. Strain signal at the passage of the first axle

Decimating the original signal sampled at 1.2 kHz simulates a reduction in sampling rate to validate the theoretical and numerical analysis [92]. Figure 34 shows the result from digital signal processing for an equivalent sampling rate of 600 Hz, 400 Hz, 300 Hz, 200 Hz, 100 Hz, 50 Hz, and 25 Hz. It is evident that the reduction of sampling rate introduces significant signal distortion and attenuation. For instance, the peak strain differs significantly from the original signal when the sampling rate decreases below the fundamental frequency of 100 Hz.

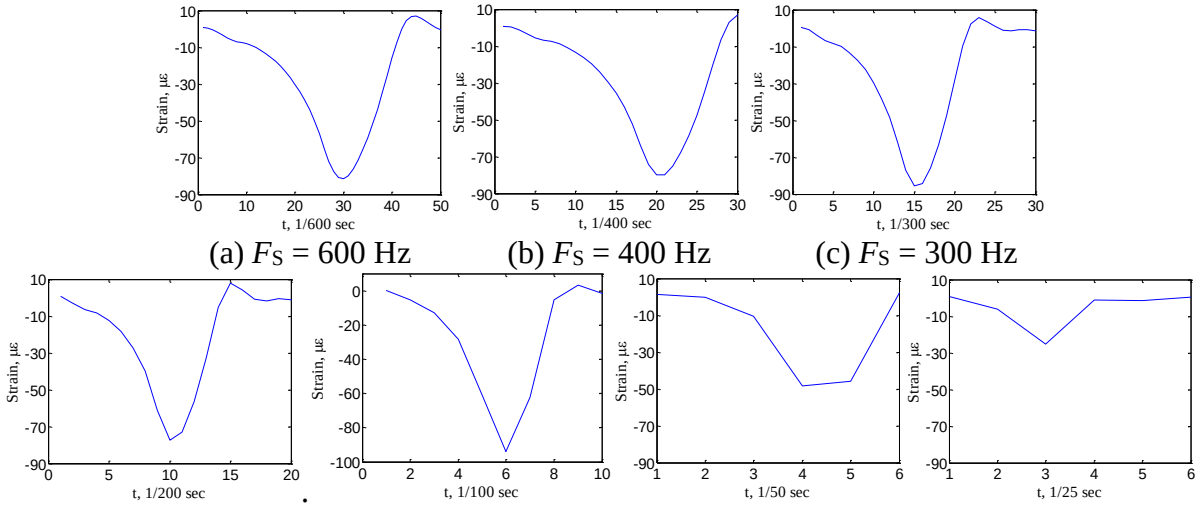

(a) F_S = 600 Hz (b) F_S = 400 Hz (c) F_S = 300 Hz

(d) F_S = 200 Hz (e) F_S = 100 Hz (f) F_S = 50 Hz (g) F_S = 25 Hz

Figure 34. Strain signal after digital filtering at different sampling rates

Table 10 compares the errors at various sampling frequencies for the field test and the numerical simulation. The measured strain at F_S = 1.2 kHz from field tests is 82.76 με and that from the numerical simulation is 77.88 με. The difference is only 5.9% and hence validates the theory. The slight differences between the two error trends account for the simplification that used rectangular functions for the boundary conditions of the concrete pavement panel.

Table 10 also indicates that at F_S = 100 Hz, the measured relative error of 22% is very close to the theoretical derivation of 17%. For the case of F_S = 200 Hz, the relative error is only 1% different from that of the theoretical derivation. Thus, if an error of 25% were practically tolerant, then a sampling frequency of 100 Hz would be suitable for collecting data from a 39 mph traversal. Increasing the sampling rate to 200 Hz reduces the error to 10%. Consequently, Table 10 guides the practical tradeoff for installations using the setup of this field study. Similarly, Table 9 extends that guidance for a range of traversal speeds.

Table 10. Peak values of the first pulses at different sampling rates.

	F_S, Hz	1200	600	400	300	200	100	50	25
Field tests	Peak value, με	82.76	81.36	79.82	85.41	77.24	94.02	48.14	25.25
	Relative error	-	2%	2%	7%	10%	22%	49%	48%
Numerical analysis	Peak value, με	77.88	79.70	82.49	84.11	86.07	91.07	67.57	37.46
	Relative error	0.4%	2.7%	6.3%	8.4%	11.0%	17.4%	12.9%	51.7%

4.5. Summary

This Chapter provides transportation researchers and engineers with guidance on the design of sampling rate selection for high-speed weigh-in-motion system deployment using the developed integrated sensing system. Field experiments in a specific case study are conducted with numerical simulations to validate the theoretical development. The conclusions of this section are as follows:

1) Generally, the strain signal of in-pavement sensors from the integrated sensing system for high-speed WIM measurements is a convolution of the pressure and the sensor sensitivity functions whereby the sampling rate requirement will be twice that of the resulting strain signal's bandwidth.

2) Higher sampling frequency increases the measurement accuracy but also significantly increases the measurement data processing and storage needs. The specific case study of this analysis illustrates the trade-off by driving a truck at 39 mph across the sensor. Numerical and experimental analysis indicates that a sample frequency of 100 Hz yields a relative measurement error of 17% and 22% respectively. Doubling the sample frequency to 200 Hz reduces the error to 10%.

3) The required sampling rate for the strain sensors should consider a trade-off between the signal-to-noise ratio and pulse distortion of the strain signal. The sampling frequency must be sufficiently high to reduce the pulse distortion while minimizing the reduction of the

SNR. The scenario of this case study found that 150 Hz represented the best tradeoff for practical application.

5. SYSTEM OPTIMIZATION

From Chapter 3 and 4, it can be seen that the developed integrated sensing system is capable of measuring WIM as well as monitoring road condition and roughness. However, for a cost-effective WIM measurement without interference from the road condition and roughness monitoring, it is required to have system optimization to achieve an ultimate effectiveness. This Chapter then presents a comprehensive framework for system optimization and introduces the procedures to achieve the optimization through the case study introduced in previous chapters. In this chapter, to accommodate a real traffic in future, a continuous axle loading at a variable axle spacing is used to simulate the real traffic loading condition. Thus, we do not assume a single axle load as in Chapter 4, which significantly extend the capability of WIM derived in Chapter 4 for future real traffic applications.

5.1. Methodology

5.1.1. System design framework

Figure 35 illustrates the developed framework for optimizing the design of the integrated sensing system for WIM measurements in this study. The parameters in the oval and square shapes are the independent and dependent variables, respectively. The optimal design must first identify parameters of the target application such as the maximum vehicle speed and the range of axle weights to be measured. The framework will then guide the remainder to the design to determine bounds of the system performance such as measurement errors and resolution.

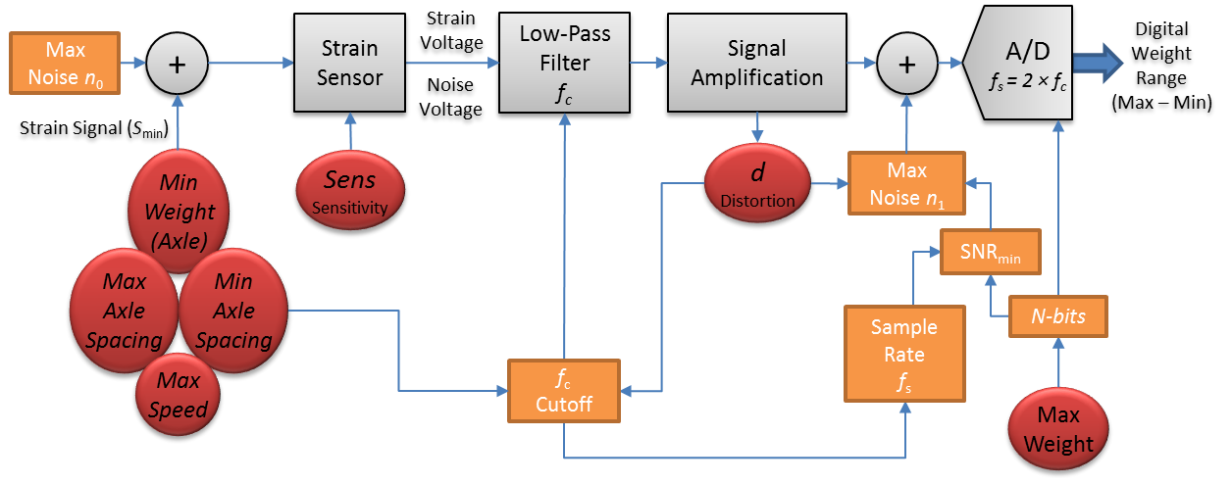

Figure 35. Flowchart of the optimal system design.

Selecting the number of analog-to-digital (A/D) converter bits (*n*-bits) establishes the system resolution, subject to achieving an input noise level and distortion that satisfies the minimum required signal-to-noise ratio (SNR_{min}) at the input of the selected A/D converter. The in-pavement strain sensors in the integrated system produce the minimum input signal S_{min} when measuring the minimum desired weight W_{min}. The sensor signal amplification prior to the A/D converter must set S_{min} to the single bit quantization level of the A/D converter. If the sensitivity function of the weight sensor is linear throughout its dynamic range, then it is characterized by a single number *Sens*. Subsequently, the sensitivity translates the single bit signal level to the minimum weight that the system can measure where

$$W_{min} = S_{min} Sens. \tag{30}$$

Subtracting SNR_{min} from S_{min} determines the maximum A/D input noise. The deconvolution of the sensor signal through the amplification and the analog low-pass filtering then establishes the maximum noise n_0 that the system can tolerate at the input of the strain sensor. The filter bandwidth is a function of the maximum vehicle speed, the minimum axle

spacing, and the number of signal harmonics to include. The latter involves a tradeoff between signal distortion and noise.

Noise n_1 at the input of the A/D converter leads to measurement inaccuracies and constrains the measurement resolution. One simplifying assumption is that the input SNR of the A/D converter is equal to its output SNR. In practice, however, A/D devices may produce additional noise such that the output SNR is lower than the input SNR.

The noise levels are not necessarily controllable. In fact, the noise from the case study's in-field integrated system discussed in previous chapters occupies many bits of the A/D converter range. Therefore, a design to accommodate noise present at the site of the in-pavement strain sensors must consider the expected maximum noise level as an independent variable that guides selection of an appropriate strain sensor, sensitivity value, and minimum measurable weight. In such a situation, the effective analog-to-digital (A/D) converter bits ($N_{\text{bits\_effective}}$) is estimated as a function of the measured SNR, SNR_{measured}, using the standard equation [93]:

$$N_{\text{bits\_effective}} = \frac{SNR_{\text{measured}} - 1.76}{6.02} \tag{31}$$

The quantity SNR_{measured} is determined by measuring the ratio of the full scale strain signal divided by the root-mean-squared (RMS) noise measured when there is no weight on the sensor. It includes signal distortion.

The maximum weight, W_{max}, that the system can measure is

$$W_{\max} = W_{\min} 2^{N_{\text{bits\_effective}}}. \tag{32}$$

Subsequently, the measurement resolution, R_{weight}, for the WIM system is

$$R_{\text{weight}} = W_{\max} 2^{-N_{\text{bits\_effective}}}. \tag{33}$$

Hence, the measurement resolution is identical to the minimum weight that the system can measure because of the linear sensitivity function.

Selecting the maximum vehicle speed and minimum axle spacing establishes the bandwidth requirement. This then leads to designing the filter and selecting its bandwidth. The latter involves a tradeoff between noise and signal distortion. Finally, the sampling rate is determined to support the system bandwidth. Iterations may then be required to optimize the overall solution because sampling rate selection will also affect the noise input to the A/D, which in turn will affect the weight measurement resolution of the system.

5.1.2. Theoretical derivation of system design parameters

This section details all the theoretical derivations needed to derive the parameters summarized in Figure 35, based on the sensor layout in an integrated system and maximum vehicle speed of the application. The system design parameters to be derived include the WIM signal produced by the strain sensors in the integrated system, the data acquisition sampling rate, the measurement resolution, and the weight dynamic range.

5.1.2.1. In-pavement strain signal with passing multiple axles

To derive the WIM signal produced by the in-pavement strain sensors, this study assumes that the hypothetical vehicles have a constant tire load and the vehicle axles have a constant spacing. This assumption simplifies the theoretical derivation of the strain signals for multi-axle WIM measurements without limiting their generalization. The numerical simulation in Section 3 also analyzes the cases beyond this assumption.

As it is known, the passage of a single tire load across the in-pavement strain sensor of the integrated system produces a strain signal $I(t)$, which is a convolution of the load function $P_L(t)$ and the sensitivity function $S_L(t)$ multiplied by the vehicle's speed v as derived in Chapter 4 and repeated in Equation 34.

$$I(t) = v\int_{-\infty}^{+\infty} P_L(t-\tau)S_L(\tau)\mathrm{d}\tau \tag{34}$$

The strain signal from this load, $I(t)$, is ideally a trapezoidal shape (Figure 36a). Therefore, its Fourier spectrum, $I(\omega)$, is a composite sinc function (Figure 36b). The expression of $I(\omega)$ is:

$$I(\omega) = \frac{AL_S P}{v^2} \operatorname{sinc}(\omega t_0 / \pi) \operatorname{sinc}(\omega T_0 / \pi) \tag{35}$$

where, A is the amplitude of the sensitivity function $S_L(t)$, L_S is the effective length of the load sensor, P is the magnitude of the tire load, t_0 is half the duration of the sensitivity function $S_L(t)$, and T_0 is half the duration of the load function $P_L(t)$. Vehicle traversals at a velocity of v realize the temporal functions from the spatial load and sensor functions.

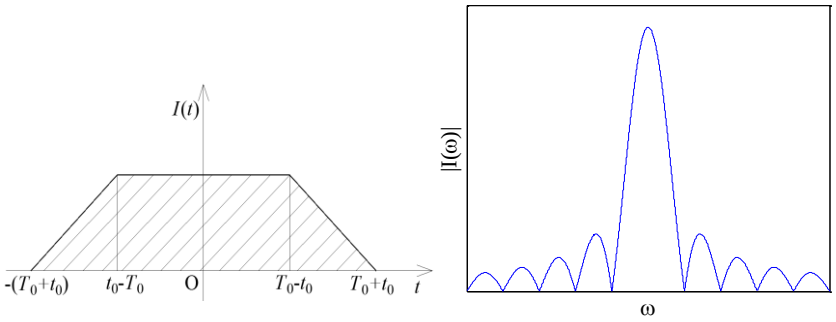

(a) $I(t)$ (b) $I(\omega)$

Figure 36. Strain signal from a single tire load and its Fourier magnitude spectrum.

When multiple axles passing the in-pavement strain sensors in the integrated system, the sensor thus produces a periodic strain signal, $\bar{I}(t)$, that results from the continuous crossing of equally spaced loading tires, as shown in Figure 37a. T_1 is the time interval between adjacent axles. The expression for the periodic strain signal, $\bar{I}(t)$, can be derived as:

$$\bar{I}(t) = \sum_{k=-\infty}^{\infty} I(t + kT_1), k = 0, \pm 1, \pm 2, \ldots \tag{36}$$

According to the principle of continuous time Fourier transform (CTFT), the spectrum of $\bar{I}(t)$ can be obtained with its Fourier coefficients a_k that is expressed in Equation 37:

$$a_k = \frac{1}{T_1} I(k\omega_1) \tag{37}$$

For $\omega_1 = 2\pi/T_1$, the Fourier transform of periodical strain signal from multi-axle vehicles, $\bar{I}(\omega)$, can be given as:

$$\bar{I}(\omega) = \sum_{k=-\infty}^{+\infty} 2\pi a_k \delta(\omega - k\omega_1) \cdot \tag{38}$$

Substituting the expression of (37) into (35) and (35) into (38) gives the final expression of the Fourier transform of periodical strain signal, $\bar{I}(\omega)$, as

$$\bar{I}(\omega) = \frac{2\pi A L_S P}{v^2 T_1} \sum_{k=-\infty}^{+\infty} \text{sinc}(k\omega_1 t_0 / \pi)\text{sinc}(k\omega_1 T_0 / \pi)\delta(\omega - k\omega_1). \tag{39}$$

Figure 37b shows the Fourier spectrum of the strain signals generated from multiple tires, $\bar{I}(\omega)$. For a periodic strain signal, $\bar{I}(t)$, its Fourier coefficient, a_k, is equally spaced samples of the Fourier transform $I(\omega)$, and its Fourier transform $\bar{I}(\omega)$ is a train of impulses occurring at the harmonically related frequencies and for which the area of the impulse at the k^{th} harmonic frequency $k\omega_1$ is 2π times the k^{th} Fourier series coefficient a_k.

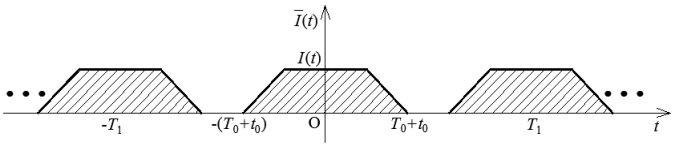

(a) $\bar{I}(t)$

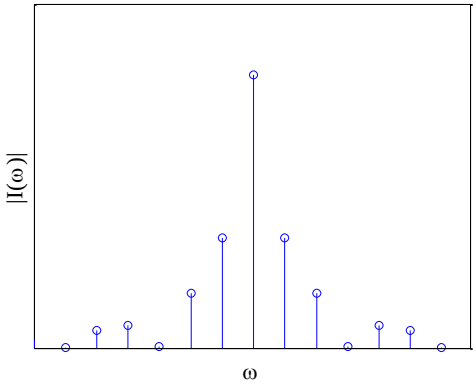

(b) $\bar{I}(\omega)$

Figure 37. Strain signal from equally spaced multiple tire loads and its Fourier spectrum.

5.1.2.2. Determination of data acquisition sampling rate for multiple axle WIM measurements

For WIM measurements of multiple axles, having a sampling rate well beyond the second or third harmonic of the continuous time signal as shown in Figure 37b will reduce the signal's distortion, as measured by the pulse width because the inclusion of higher frequency harmonics strengths the signal. However, on the other side, higher sampling rate will decrease the signal-to-noise ratio (SNR) since the inclusion of higher frequency harmonics brings more energy from noise at higher frequency at the same time. Therefore, the selection of an appropriate sampling rate, f_s, for multiple axle WIM measurement, is a tradeoff to maximize SNR and minimize signal distortion level (*Dist*), which can be determined as below:

$$f_s = f\{\text{Max}[\text{SNR}(f_s)], \text{Min}[\text{Dist}(f_s)]\}\text{c} \quad (40)$$

If the initial input strain signal is $s_0(t)$, the noise is $n_0(t)$, and the impulse response of the anti-aliasing filter is $h(t)$, then the strain signal and noise after the filter, $s_1(t)$ and $n_1(t)$, respectively is derived as:

$$s_1(t) = s_0(t)*h(t) \tag{41}$$

$$n_1(t) = n_0(t)*h(t) \tag{42}$$

where * denotes the convolution. The SNR of the input signal (SNR_0) and that of the output signal (SNR_1) can then be calculated as:

$$SNR_0 = 20*\log_{10}\frac{\mathrm{RMS}(s_0)}{\mathrm{RMS}(n_0)} \tag{43}$$

$$SNR_1 = 20*\log_{10}\frac{\mathrm{RMS}(s_1)}{\mathrm{RMS}(n_1)} \tag{44}$$

where, the function RMS() is the root mean square of a temporal signal.

5.1.2.3. Determination of dynamic range and resolution

A digital system decodes the sampled data with a bit-error-rate (BER) that is a function of the SNR at its input. A given level of acceptable BER determines a minimum SNR level, SNR_{min}, of the A/D converter. The power in dB of a noise, n_0, at the input of an anti-aliasing filter, $P_{n0,\,dB}$ is given as:

$$P_{n0,\,dB} = 20*\log_{10}\mathrm{RMS}(n_0). \tag{45}$$

After anti-alias filtering, the output noise $n_1(t)$ has the power of $P_{n1,\,dB}$:

$$P_{n1,\,dB} = 20*\log_{10}\mathrm{RMS}(n_1). \tag{46}$$

Thus, the minimum output power of the strain signal $s_1(t)$, $P_{s1,\,dB}$, must be

$$P_{s1,\,dB} = P_{n1,\,dB} + SNR_{min}. \tag{47}$$

The input strain signal of the sensor, $s_0(t)$, is derived by deconvolving after the effects of the anti-aliasing filter, $P_{s1,\,dB}$. Subsequently from Equation 30, for any maximum tolerable noise

at the input of the A/D converter, the minimum output strain signal satisfying the minimum SNR requirement corresponds to a minimum measurable tire load. The dynamic range of the scale system is then [W_{min}, W_{max}].

In summary, this section derived the theoretical strain signal of the in-pavement strain sensors of the integrated system under conditions of multiple axle tire loads, the corresponding requirement for an appropriate sampling rate, the dynamic range, and the resolution. Practitioners can use this theoretical framework to optimize and guide the design of a WIM system.

5.2. Numerical Study

This section conducts a numerical sensitivity study based on the theories established in Section 5.1 and the case study mentioned in previous chapters. The load from the first tire of the semi-truck in Figure 10, P, was used in this sensitivity analysis with a magnitude of 2,630.8 kg (5,800 lb). The vehicle speed, *v*, of 17.4 m/s (39 mph), same as in the case study, was used in the simulations. Table 11 lists all the parameters used for the numerical analysis of this Chapter which is consistent with Table 8 in Chapter 4 for the same case study. *SA* is the distance between the adjacent axles. This section followed the assumption that the tire load was a constant. Three scenarios of vehicle axle spacings, SA, were analyzed: 1.5 m (5 ft), 7.9 m (26 ft), and random values between 1.5-7.9 m (5-26 ft). The selection of the distance between axles was based on a national survey of the range of vehicles' axle spacing, which covered most of the vehicle types in United States [94]. In this simulation, it was assumed that 100 axles passed the WIM sensor. Figures 38a-c show the simulated strain signals from the passing axles of the three scenarios.

Table 11. Parameters for numerical simulation.

Parameter	Value	Unit	Parameter	Value	Unit
a	1.8	m	K	29.8×10^6	kg/m^3
b	1.8	m	x_0	1.3	m
h	0.076	m	y_0	1.1	m
L_0	0.35	m	h_0	0.07	m
B_0	0.23	m	P	2,630.8	kg
E	15000	MPa	V	17.4	m/s
μ	0.16	-	SA	1.5-7.9	m

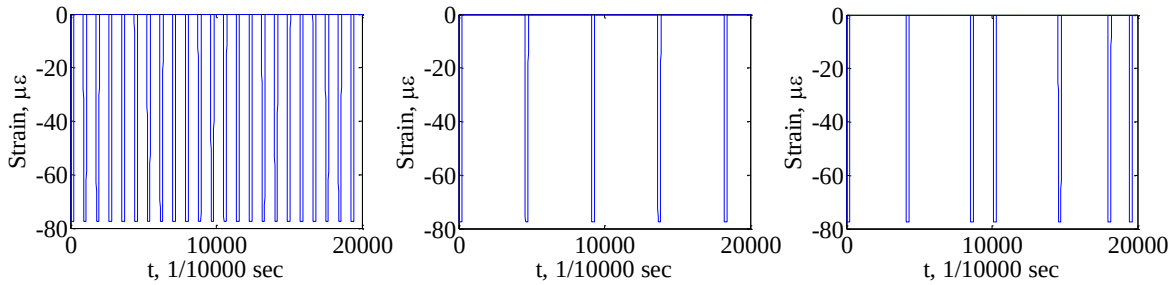

(a) SA = 1.5 m (5 ft) (b) S_A = 7.9 m (26 ft) (c) S_A = 1.5-7.9 m (5-26 ft)

Figure 38. Strain signals at different axle distances.

To analyze the influence of various sampling frequencies, this study applied a 7th order Bessel filter as the anti-aliasing filter at different cutoff frequencies, which minimized the temporal distortions in the output pulse durations. Figures 39a-c illustrate the decrease in SNR with the increase of filter cutoff frequencies for the three scenarios of different axle distances of 1.5 m (5 ft), 7.9 m (26 ft), and random values between 1.5-7.9 m (5-26 ft). For each scenario, the simulations assumed three hypothetical input noise levels, -13 dB, -3 dB, and 17 dB to highlight the expected trends of declining SNR. The three scenarios showed very little differences in between, indicating that the SNR change with cutoff frequency is not sensitive to axle distances if they are greater than 1.5 m (5 ft). Thus, for practical applications, since most vehicles on roads have axle distances larger than 1.5m (5ft), the axle distance is not a major concern for WIM

measurements, validating the assumption that a passing vehicle can be simplified as single tire load which was used by many researchers in field. In the case study performed, the axle spacing of the truck was between 1.5m to 7.9m. Therefore, Figure 39(c) also shows the SNR change with cut-off frequency for the semi-truck of the case study. From Figure 31, the actual noise level in the case study used in this study can be identified as 17.0 dB.

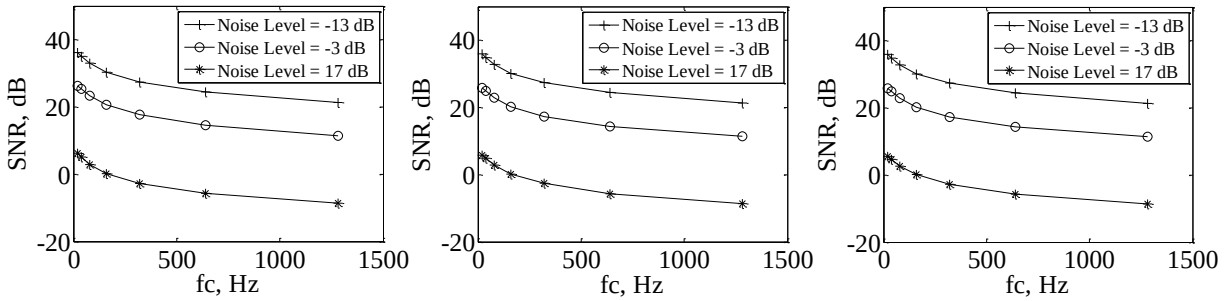

(a) S_A = 1.5 m (5 ft) (b) S_A = 7.9 m (26 ft) (c) S_A = 1.5-7.9 m (5-26 ft)

Figure 39. Signal to noise ratio at different cutoff frequencies.

The distortion levels of the strain signals of the three different scenarios of vehicle axle spaces were also analyzed by measuring the pulse width at the center of the signal series. This analysis measured the pulse width at the average signal level between the maximum and the minimum of the pulse train. Figures 40a-c show the changes of pulse width vs cutoff frequency for the three cases of axle spacing, respectively. It is noteworthy that an increase in cutoff frequency causes a decrease in pulse width or distortion level, validating the theoretical analysis developed in Section 5.2. That is, the increase of the filter cutoff frequency reduces distortion by trading off the output SNR. The figures also indicate that at 160 Hz, all the three scenarios showed a trend of diminishing of return. Since in the case study, the axle spacing of the truck was within 1.5m to 7.9m, from Figure 40(c), it is known that for the case study in this study, the cutoff frequency of the anti-aliasing filter is required to be 160 Hz or higher.

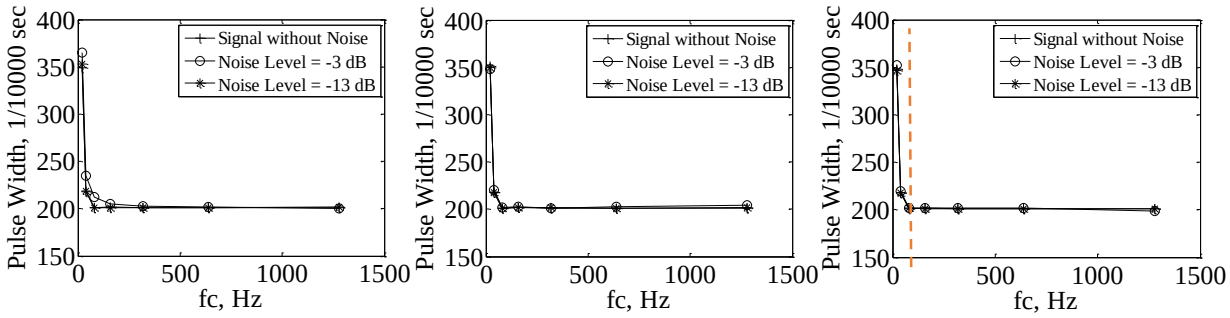

(a) S_A = 1.5 m (5 ft) (b) S_A = 7.9 m (26 ft) (c) S_A = 1.5-7.9 m (5-26 ft)

Figure 40. Pulse width at different cutoff frequencies.

Figure 41 shows the filtered signals of the passing semi-truck signals after the anti-aliasing filter with cut-off frequencies of 160 Hz. When compared with Figure 41 of the original signal with sampling frequency of 1.2 kHz, it is clearly demonstrated that a cut-off frequency will be sufficient in this study for the anti-aliasing filter to meet the trade-off for high SNR and low distortion level as expected.

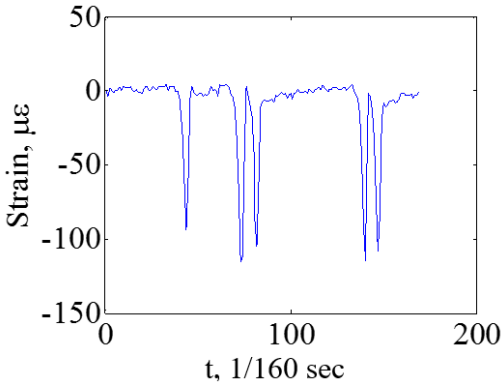

Figure 41. Filtered signals from the case study with cut-off frequencies of 160 Hz.

Figures 42a and 42b respectively plot the minimum input signal power and the minimum tire weight for a presumed value of SNR_{min} = 74 dB at the selected cutoff frequency of the anti-aliasing filter, 160 Hz, for the three scenarios of different axle spaces. The power of the minimum signal in dB has a linear relationship with the power of the noise in dB, validating the

theoretical derivation in Section 5.1. This result also indicates that the minimum detectable tire weight increases by 12.2% for each dB decrease of the input noise power. Figure 42b also shows how the axle distances influence the minimum detectable weight of the WIM system. For the same noise level, the minimum detectable weight is smaller for the shorter axle spacing because the power of the signal is greater than that for the intermediate and wider axle spaces. It is worth noting here that both the weight and spacing of vehicle axles contribute to the signal power, and therefore determine the signal quality or allowable noise level. Thus, from Figure 42b, it can be seen that the WIM system in the case study of this study, would yield to a minimum detectable tire weight of $6*10^8$ lbs for a 74dB noise level.

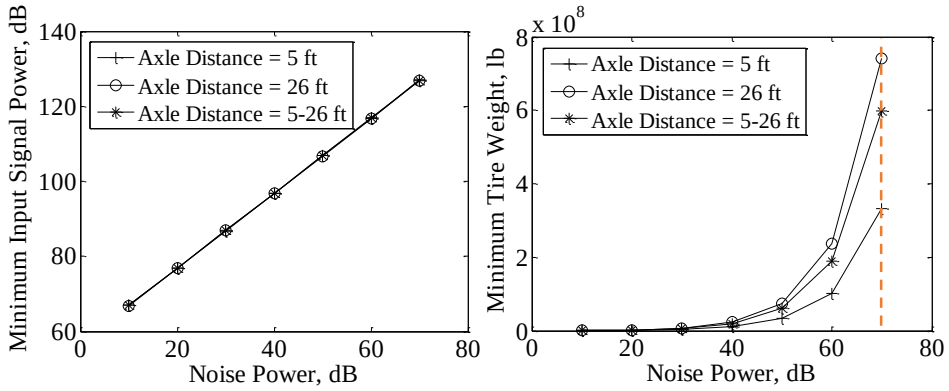

(a) Minimum input signal power (b) Minimum tire weight

Figure 42. Minimum identifiable signal at different noise power levels for SNR_{min} = 74 dB.

Figure 43 shows that the minimum weight change with cutoff frequency for four different input noise levels, -10 dB, 0 dB, 10 dB, and 20 dB, for the case study with random axle spacing between 1.5m (5 ft) and 7.9m (26 ft). It can be seen that the minimum detectable tire weight generally increases with the cutoff frequency at different input noise levels. The increase is due to the additional noise as the cutoff frequency increases. It is evident that the filter has a greater impact at the higher input noise levels. If the cut-off frequency is set as 160 Hz, the minimum

measurable tire weight is 0.04, 0.14, 0.63, and 1.95 million pounds for noise level at -10dB, 0dB, 10dB, and 20dB.

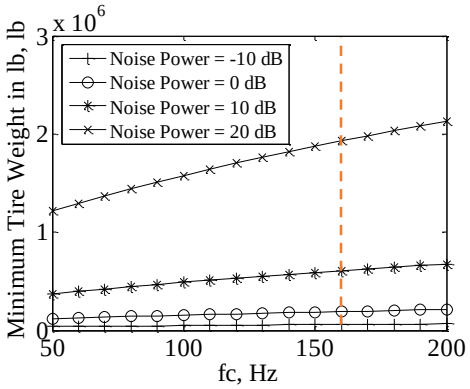

Figure 43. Minimum identifiable weight at different cutoff frequencies for 1.5-7.9 m (5-26 ft) random axle distances.

5.3. System implementation

This section evaluates an implementation using the optimal system design procedure established in previous sections, and uses parameters measured from the case study of the integrated system installed at the MnROAD facility as introduced in previous chapters.

The WIM system design of the case study set the number of A/D bits to be 8-bits because of its common availability. The weight resolution of the optimal integrated system can then be calculated as:

$$R_{\text{weight}} = W_{\max}/2^{N\text{-bit}} \tag{48}$$

The full scale of the strain signal input at the A/D is 157 με in this case study yielding a maximum measurable weights of 4,989.5 kg (11,000 lb). According to Equation (48), the minimum measurable weight or weight resolution of the WIM system yields to 19.5 kg (43 lb) in the case study.

The measured sensitivity of the installed WIM sensor is 0.03 με/kg (0.014 με/lb) [95]. Hence, the strain signal level from the minimum weight can be calculated following Equation

(46) as -4.2 dB. The minimum SNR requirement of the A/D was 49.9 dB from Equation (49). This dictated a maximum tolerable noise level at the A/D input:

$$SNR_{\min} = N\text{-bit} \cdot 6.02 + 1.76 \tag{49}$$

Thus, the $SNR_{\min}$ of this case study is -54.2 dB from Equation (49). The sampling rate for the installed WIM system was 1,200 Hz. By the Nyquist Theorem, the bandwidth should be no greater than 600 Hz. The sensitivity study in Section 5.2 determined that 160 Hz was the best cutoff frequency for the analog anti-aliasing filter. Therefore, the fractional noise equivalent bandwidth of the system can be obtained as below:

$$B_f = f_c/BW \tag{50}$$

which is calculated to be 160Hz/600Hz = 0.267 for the case study.

The noise reduction can then be calculated as:

$$N_{\text{reddB}} = 20 \cdot \log(B_f) \tag{51}$$

which gives -11.5 dB in this case.

Therefore, the maximum tolerable noise before the anti-aliasing filter is -54.2 – (-11.5) = -42.7 dB. From the number of bits and sensor sensitivity, the equivalent weight error for this integrated system can be expressed as:

$$E_{\text{weight}} = W_{\max}/2^{N\text{-bit}+1} \tag{52}$$

which yields to ± 9.8 kg (21.5 lb) for this case study.

However, from Figure 39, it can be seen that the SNR measured at the output of A/D is 14 dB, and the signal level is 38.4 dB. The actual noise has 38.4 – 14 = 24.4 dB, which equals to 16.5 με. The noise level can then be obtained as:

$$Bits_n = \ln(N_{\text{dB}})/\ln(2) \tag{53}$$

Thus, for the installed WIM sensor in the case study, the noise occupied 4 bits of the bandwidth. The noise before the anti-aliasing filter was 35.8 dB, which corresponded to 61.9

με. This noise level was much greater than the maximum tolerable level of 24.4 dB corresponding to 16.5 με which is established earlier. Therefore, the analysis performed here demonstrated that the noise level at the transducer prevented the integrated system in the case study from providing the expected resolution for WIM measurements. Advanced solutions of transducers with less noise are needed for an optimal system. From this section, it is clearly demonstrated that the developed system design framework in this study can identify problems of an integrated system for WIM measurements so that users can resolve the problems and achieve an optimal WIM system.

5.4. Summary

This chapter developed a comprehensive framework for optimal the integrated sensing system design for WIM measurements. It derived the relationships between the sampling rate, resolution, SNR, sensor sensitivity, and the dynamic range of the WIM weight scale. The approach provided a solution for future integrated system to select the sampling rate of the data capture equipment, determine the dynamic range of the weight measurement scale, and establish the tolerable noise levels. The theoretical analysis and numerical simulations of the case study provide a template for future integrated system designs for WIM measurements and sensor parameter selection.

6. CONCLUSIONS AND FUTURE WORK

This dissertation designed an integrated monitoring system for simultaneous road condition monitoring and weigh-in-motion (WIM) measurements using in-pavement strain sensors. It presented a robust sensing system based on the GFRP packaged FBG sensors including several 1D and 3D GFRP-FBG sensors, and strain gauges. A case study performed at MnROAD facility, MnDOTshowed that the developed sensing system monitors the behavior of the concrete pavement under short-term vehicle load and environmental impact. It served as an approach for pavement's structural health monitoring. Meanwhile, it collected the information about road roughness and ride quality of the road sections by virtue of the relationship between the strain distribution and the pavement deformation. The WIM sampling analysis and system optimization could provide guidance on future WIM measurements using in-pavement strain sensors with respect to sampling rate, resolution, noise disturbance, and weight scale. The conclusions of this dissertation study include:

1) This study presents an innovative robust integrated sensing system based on in-pavement strain sensors for simultaneous road condition and traffic monitoring. The integrated system includes an implementation of at least three in-pavement strain sensors and one temperature sensor. The developed integrated sensing systems were deployed at MnROAD facility, MnDOT, for a case study to validate its performance.

2) This study provides transportation researchers and engineers with a cost-effective method of road condition assessment and roughness evaluation using the integrated sensing system deployed inside the pavement. Field studies approve that the integrated sensing system is capable to detect the early performance of the instrumented pavements for road condition assessments. The sensors monitored the reopening behavior of existing cracks

and joints and the cracking of adjacent pavement panel. In addition, the strains obtained from the integrated system can be used to derive the roughness of the instrumented road section theoretically for road roughness evaluation. Numerical simulation proves that the integrated sensing system is able to measure the road roughness with a measurement accuracy of 80% or higher at a specific sensor implementation interval of 0.7 m or shorter for the roughness levels that are of most concern to agencies and this approach is relatively insensitive to the noise disturbances. The case studies validated the new roughness evaluation method based on the integrated sensing system by comparing the consistency of its proportionality with a connected-vehicle method of roughness characterization that is directly proportional to the IRI. This new method will provide roadway agencies with the ability to evaluate road condition and roughness in real time and continuously throughout the service life of the road to enable improved methods of predictive asset management, and the potential for significant lifetime cost savings.

3) This study provides transportation researchers and engineers with guidance on the design of sampling rate selection for high-speed weigh-in-motion system deployment using the developed integrated sensing system. Field experiments in a specific case study are conducted with numerical simulations to validate the theoretical development. Generally, the strain signal of in-pavement sensors from the integrated sensing system for high-speed WIM measurements is a convolution of the pressure and the sensor sensitivity functions whereby the sampling rate requirement will be twice that of the resulting strain signal's bandwidth. Thus, a travelling speed of 80 mph requires a sampling rate of 204 Hz for an accuracy of 85% based on the example study conditions. Higher sampling frequency increases the measurement accuracy but also significantly increases the

measurement data processing and storage needs. Numerical and experimental analysis indicates that a sample frequency of 100 Hz yields a relative measurement error of 17% and 22% respectively. Doubling the sample frequency to 200 Hz reduces the error to 10%. The required sampling rate for the strain sensors should consider a trade-off between the signal-to-noise ratio and pulse distortion of the strain signal. The sampling frequency must be sufficiently high to reduce the pulse distortion while minimizing the reduction of the SNR. The scenario of this case study found that 150 Hz represented the best tradeoff for practical application. The outcome of this research can serve as a reference for future WIM activities. The required sampling rate for high-speed weigh-in-motion installations is directly proportional to the maximum traversal speed that it must accommodate.

4) At last but not least, this study develops a comprehensive framework for optimal the integrated sensing system design for WIM measurements. It derived the relationships between the sampling rate, resolution, SNR, sensor sensitivity, and the dynamic range of the WIM weight scale. The approach provides a solution for future WIM designs to select the sampling rate of the data capture equipment, determine the dynamic range of the weight measurement scale, and establish the tolerable noise levels. The theoretical analysis and numerical simulations of the case study provide a template for future WIM system designs and sensor parameter selection. An system implementation shows that the case with a noise component occupying 4 bits of the 8-bit A/D converter requires a better signal transducer to increase the signal to noise ratio.

Future work will be remaining to refine the integrated monitoring system through theoretical and numerical analysis, practical field testing, and signal processing, including:

1) Application of the integrated monitoring system on traffic data collection and analysis. Weigh-in-motion is one aspect of traffic data collection. The extension of the integrated monitoring system onto other aspects, e.g. vehicle counting and vehicle classification, would broaden the application of the system.
2) Improvement of the system by real traffic data. This study conducted all the field testing on the research road section at MnROAD facility, MnDOT. It lacks the validation and further improvement using real traffic and vehicle loading.

REFERENCES

1. Mertz, L., *Origins of the Interstate.* on the website of the US Dept. of Transportation, www. fhwa. dot. gov/intrastructure/origin. pdf, 1986.

2. Cheng, H.-D. and M. Miyojim, *Automatic pavement distress detection system.* Information Sciences, 1998. **108**(1): p. 219-240.

3. Bam. Available from: http://www.bam.de.

4. Potter, J., H. Mayhew, and A. Mayo, *Instrumentation of the Full-scale Experiment on A1 Trunk Road at Conington, Huntingdonshire.* Rrl Reports, Road Research Lab/UK/, 1969.

5. Sebaaly, P., et al., *Instrumentation for flexible pavements—Field performance of selected sensors.* Federal Highway Administration, Washington, DC, 1991.

6. Sebaaly, P., N. Tabatabaee, and B. Kulakowski, *Evaluation of the Hall Effect sensor for pavement instrumentation.* Journal of testing and evaluation, 1995. **23**(3): p. 189-195.

7. Hipley, P. *Caltran's current state-of-practice*. in *Proceedings of the Instrumental Systems for Diagnostics of Seismic Response of Bridges and Dams*. 2001.

8. Huff, R., C. Berthelot, and B. Daku, *Continuous primary dynamic pavement response system using piezoelectric axle sensors.* Canadian journal of civil engineering, 2005. **32**(1): p. 260-269.

9. Xue, W. and E. Weaver, *Pavement shear strain response to dual and wide-base tires.* Transportation Research Record: Journal of the Transportation Research Board, 2011(2225): p. 155-164.

10. Lajnef, N., et al., *Toward an integrated smart sensing system and data interpretation techniques for pavement fatigue monitoring.* Computer‐Aided Civil and Infrastructure Engineering, 2011. **26**(7): p. 513-523.

11. Davis, M. and A. Kersey, *All-fibre Bragg grating strain-sensor demodulation technique using a wavelength division coupler.* Electronics Letters, 1994. **30**(1): p. 75-77.

12. Hirayama, N. and Y. Sano, *Fiber Bragg grating temperature sensor for practical use.* ISA transactions, 2000. **39**(2): p. 169-173.

13. Maaskant, R., et al., *Fiber-optic Bragg grating sensors for bridge monitoring.* Cement and Concrete Composites, 1997. **19**(1): p. 21-33.

14. Mufti, A.A., *Structural health monitoring of innovative Canadian civil engineering structures.* Structural Health Monitoring, 2002. **1**(1): p. 89-103.

15. Chauhan, M. and E. Sharma, *A Special Fiber Optic Sensor for Measuring Wheel Loads of Vehicles on Highways.* International Journal of Research, 2014. **1**(11): p. 1272-1283.

16. Li, H.-N., D.-S. Li, and G.-B. Song, *Recent applications of fiber optic sensors to health monitoring in civil engineering.* Engineering structures, 2004. **26**(11): p. 1647-1657.

17. Wang, J.-N. and J.-L. Tang, *Using Fiber Bragg Grating Sensors to Monitor Pavement Structures.* Transportation Research Record: Journal of the Transportation Research Board, 2005(1913): p. 165-176.

18. Udd, E. and W.B. Spillman Jr, *Fiber optic sensors: an introduction for engineers and scientists* 2011: John Wiley & Sons.

19. Zhou, Z., et al., *Techniques of Advanced FBG Sensors: Fabrication, Demodulation, Encapsulation, and Their Application in the Structural Health Monitoring of Bridges.* Pacific Science Review, 2003. **5**(1): p. 116-121.

20. Zhou, Z., J. Ou, and B. Wang. *Smart FRP-OFGB bars and their application in reinforced concrete beams*. in *Proceedings of the first international conference on structural health monitoring and intelligent structure*. 2003. Tokyo, Japan.

21. Timm, D.H., A.L. Priest, and T.V. McEwen, *Design and instrumentation of the structural pavement experiment at the NCAT test track* 2004: National Center for Asphalt Technology, Auburn University.

22. Lukanen, E., *Load testing of instrumented pavement sections.* 2005.

23. Al-Qadi, I.L., et al., *The Virginia SMART ROAD: the impact of pavement instrumentation on understanding pavement performance (with discussion).* Journal of the Association of Asphalt Paving Technologists, 2004. **73**.

24. Loulizi, A., I.L. Al-Qadi, and M. Elseifi, *Difference between in situ flexible pavement measured and calculated stresses and strains.* Journal of transportation engineering, 2006. **132**(7): p. 574-579.

25. Komsa. Available from: http://komsa.com.tr.

26. ASTM, *E867 Standard Terminology Relating to Vehicle-Pavement Systems*, 2012, American Society for Testing Materials, ASTM.

27. Abaynayaka, S., et al., *Tables for estimating vehicle operating costs on rural roads in developing countries.* 1976.

28. Brickman, A.D., et al., *Road Roughness Effects on Vehicle Performance*, 1972.

29. Gillespie, T. and M. Sayers, *Role of Road Roughness in Vehicle Ride*, in *60th Annual Meeting of the Transportation Research Board* 1981, Transportation Research Board: Washington District of Columbia, United States. p. 15-20.

30. Van Deusen, B.D., *Analytical techniques for designing riding quality into automotive vehicles*, 1967, SAE Technical Paper.

31. Saleh, M.F., M.S. Mamlouk, and E.B. Owusu-Antwi, *Mechanistic roughness model based on vehicle-pavement interaction.* Transportation Research Record: Journal of the Transportation Research Board, 2000. **1699**(1): p. 114-120.

32. Klaubert, E.C., *Highway Effects on Vehicle Performance*, 2001.

33. ASTM, *E1926 Standard Practice for Computing International Roughness Index of Roads from Longitudinal Profile Measurements*, 2008, American Society for Testing Materials, ASTM.

34. Marcondes, J., et al., *Spectral analysis of highway pavement roughness.* Journal of transportation engineering, 1991. **117**(5): p. 540-549.

35. Smith, K., et al., *Smoothness specifications for pavements*, 1997.

36. ASTM, *E1489 Standard Practice for Computing Ride Number of Roads from Longitudinal Profile Measurements Made by an Inertial Profile Measuring Device*, 1998, American Society for Testing Materials, ASTM.

37. McKenzie, D. and M. Srinarawat, *Root Mean Square Vertical Acceleration (RMSVA) as a Basis for Mays Meter Calibration.* Center for Transportation Research, Univ. of Texas at Austin, Brazil Project Tech. Memo BR-23, 1978.

38. Huang, Y.H., *Pavement analysis and design* 1993.

39. Brown, D., W. Liu, and T. Henning, *Identifying pavement deterioration by enhancing the definition of road roughness* 2010.

40. Spangler, E.B. and W.J. Kelly, *GMR road profilometer-a method for measuring road profile.* Highway Research Record, 1966.

41. NCHRP, *Measuring, Characterizing, and Reporting Pavement Roughness of Low-Speed and Urban Roads*, 2013, Transportation Research Board.

42. Hyman, W.A., et al., *Improvements in data acquisition technology for maintenance management systems* 1990.

43. McGhee, K.H., *Automated pavement distress collection techniques*. Vol. 334. 2004: Transportation Research Board.

44. American Association of State Highway, and Transportation Officials, *AASHTO Guide for Design of Pavement Structures, 1993*. Vol. 1. 1993: AASHTO.

45. Prozzi, J.A. and F. Hong, *Effect of weigh-in-motion system measurement errors on load-pavement impact estimation.* Journal of Transportation Engineering, 2007. **133**(1): p. 1-10.

46. Austroads, *Weigh-in-motion Technology*, 2000, Austroads: Sydney, Australia.

47. Hopkins, R., *Weighing vehicles in motion.* Highway Research Board Bulletin, 1952(50).

48. George, Y. and C. Antoniou, *Integration of weigh-in-motion technologies in road infrastructure management.* Institute of Transportation Engineers. ITE Journal, 2005. **75**(1): p. 39.

49. Lu, Q., et al., *Truck traffic analysis using weigh-in-motion (WIM) data in California.* University of California, Berkeley, Institute of Transportation Studies, Pavement Research Center, Berkeley, California, USA, 2002.

50. American Society for Testing and Materials, *Standard specification for highway weigh-in-motion (WIM) systems with user requirements and test methods*,, in ASTM Standard E1318-091994.

51. Sharma, S.C., G. Stamatinos, and J. Wyatt, *Evaluation of IRD-WIM-5000-a Canadian weigh-in-motion system.* Canadian journal of civil engineering, 1990. **17**(4): p. 514-520.

52. Stephens, J., Y. Qi, and D. Veneziano, *Montana Weigh-in-Motion (WIM) and Automatic Traffic Recorder (ATR) Strategy*, 2013, Montana Department of Transportation Helena, MT.

53. Cheng, L., H. Zhang, and Q. Li, *Design of a capacitive flexible weighing sensor for vehicle WIM system.* Sensors, 2007. **7**(8): p. 1530-1544.

54. Malla, R.B., A. Sen, and N.W. Garrick, *A special fiber optic sensor for measuring wheel loads of vehicles on highways.* Sensors, 2008. **8**(4): p. 2551-2568.

55. Yuan, S., et al., *Optic fiber-based dynamic pressure sensor for WIM system.* Sensors and Actuators A: Physical, 2005. **120**(1): p. 53-58.

56. Teral, S.R., et al. *Fiber optic weigh-in-motion sensor: correlation between modeling and practical characterization*. in *1996 Symposium on Smart Structures and Materials*. 1996. International Society for Optics and Photonics.

57. Muhs, J.D., et al. *Results of a portable fiber optic weigh-in-motion system*. in *OE Fiber-DL tentative*. 1991. International Society for Optics and Photonics.

58. Tobin Jr, K.W. and J.D. Muhs. *Algorithm for a novel fiber optic weigh-in-motion sensor system*. in *Specialty Fiber Optic Systems for Mobile Platforms*. 1991. International Society for Optics and Photonics.

59. Zhang, W., C. Suo, and Q. Wang, *A novel sensor system for measuring wheel loads of vehicles on highways.* Sensors, 2008. **8**(12): p. 7671-7689.

60. Bushman, R. and A.J. Pratt. *Weigh in motion technology-Economics and performance*. in *Presentation on the North American Travel Monitoring Exhibition and Conference (NATMEC). Charlotte, North Carolina*. 1998.

61. Loshbough, R.C. and D.L. Hall, *Vehicle weighing in motion apparatus and method*, 1991, Google Patents.

62. FHWA-NJ, *Implementation of Weigh-in-Motion (WIM) Systems*, 2009, FHWA-NJ: Piscataway, NJ.

63. Gagarine, N., I. Flood, and P. Albrecht. *Weighing trucks in motion using Gaussian-based neural networks*. in *Neural Networks, 1992. IJCNN., International Joint Conference on*. 1992. IEEE.

64. Hill, D.J., P.J. Nash, and N. Sanders. *Vehicle weigh-in-motion using multiplexed interferometric sensors*. in *Optical Fiber Sensors Conference Technical Digest, 2002. Ofs 2002, 15th*. 2002.

65. Lechner, B., et al., *A wavelet-based bridge weigh-in-motion system.* International Journal on Smart Sensing and Intelligent Systems, 2010. **3**(4): p. 573-591.

66. Lynch, J.P., et al., *Performance monitoring of the Geumdang Bridge using a dense network of high-resolution wireless sensors.* Smart Materials and Structures, 2006. **15**(6): p. 1561.

67. Ko, J. and Y. Ni, *Structural health monitoring and intelligent vibration control of cable-supported bridges: Research and application.* KSCE Journal of Civil Engineering, 2003. **7**(6): p. 701-716.

68. Kim, J. and J.P. Lynch, *Experimental analysis of vehicle–bridge interaction using a wireless monitoring system and a two-stage system identification technique.* Mechanical Systems and Signal Processing, 2012. **28**: p. 3-19.

69. Zhou, Z., et al., *Optical fiber Bragg grating sensor assembly for 3D strain monitoring and its case study in highway pavement.* Mechanical Systems and Signal Processing, 2012. **28**: p. 36-49.

70. Yin, S.S. and P. Ruffin, *Fiber optic sensors* 2002: Wiley Online Library.

71. Burnham, T. *Thin concrete pavements and overlays—ongoing MnROAD research*. in *MnDOT, Presented in 2013 NCC Spring Meeting, Philadelphia, PA*. 2013.

72. Huang, Y. and M.a.A.-T. Muapos, *Glass fiber-reinforced polymer packaged fiber Bragg grating sensors for low speed weight-in-motion measurements.* Optical Engineering, 2016: p. OE-160542P.

73. Karamihas, S.M., M.A. Barnes, and R.O. Rasmussen, *Pavement surface specification for road load measurement.* 2014.

74. Timoshenko, S., S. Woinowsky-Krieger, and S. Woinowsky-Krieger, *Theory of plates and shells*. Vol. 2. 1959: McGraw-hill New York.

75. Jiang, C.D., et al. *Simulation of Road Roughness Based on Using IFFT Method*. in *Software Engineering (WCSE), 2012 Third World Congress on*. 2012. IEEE.

76. Wu, J.-J., *Simulation of rough surfaces with FFT.* Tribology International, 2000. **33**(1): p. 47-58.

77. Bender, C.M. and S.A. Orszag, *Advanced mathematical methods for scientists and engineers I: Asymptotic methods and perturbation theory*. Vol. 1. 1999: Springer.

78. Andren, P., *Power spectral density approximations of longitudinal road profiles.* International Journal of Vehicle Design, 2006. **40**(1): p. 2-14.

79. Cebon, D., *Handbook of vehicle-road interaction* 1999.

80. Sayers, M.W. and S.M. Karamihas, *The little book of profiling.* Ann Arbor: Transportation Research Institute, University of Michigan. http://www. umtri. umich. edu/erd/roughness/lit_book. pdf, 1998.

81. Bridgelall, R. *A participatory sensing approach to characterize ride quality*. in *SPIE Smart Structures and Materials+ Nondestructive Evaluation and Health Monitoring*. 2014. International Society for Optics and Photonics.

82. Bridgelall, R., *Inertial Sensor Sample Rate Selection for Ride Quality Measures.* Journal of Infrastructure Systems, 2014.

83. Zhang, Z., et al. *Field validation of road roughness evaluation using in-pavement strain sensors*. in *SPIE Smart Structures and Materials+ Nondestructive Evaluation and Health Monitoring*. 2016. International Society for Optics and Photonics.

84. Bochner, S. and K. Chandrasekharan, *Fourier transforms* 1949: Princeton University Press.

85. Robert, J.M., *Introduction to Shannon Sampling and Interpolation Theory* 1991, New York: Springer-Verlag.

86. Mishra, R.C. and S.K. Chakrabarti, *Rectangular plates resting on tensionless elastic foundation: some new results.* Journal of engineering mechanics, 1996. **122**(4): p. 385-387.

87. Timoshenko, S. and S. Woinowsky-Krieger, *Theory of Plates and Shells*, 1959, Mcgraw-Hill College: New York.

88. Choi, Y.H. *Gated UWB pulse signal generation*. in *Ultra Wideband Systems, 2004. Joint with Conference on Ultrawideband Systems and Technologies. Joint UWBST & IWUWBS. 2004 International Workshop on*. 2004. IEEE.

89. Zhang, Z., et al., *Glass fiber–reinforced polymer–packaged fiber Bragg grating sensors for ultra-thin unbonded concrete overlay monitoring.* Structural Health Monitoring, 2015. **14**(1): p. 1475921714554143.

90. Wikibooks, *A-level Computing/AQA/Problem Solving, Programming, Data Representation and Practical Exercise/Fundamentals of Data Representation/Sampled sound*, 2012.

91. Thomson, W., *Delay networks having maximally flat frequency characteristics.* Proceedings of the IEE-Part III: Radio and Communication Engineering, 1949. **96**(44): p. 487-490.

92. Lathi, B.P. and R.A. Green, *Essentials of Digital Signal Processing* 2014: Cambridge University Press.

93. Kester, W., *Understand SINAD, ENOB, SNR, THD, THD+ N, and SFDR so you don't get lost in the noise floor.* MT-003 Tutorial, www. analog. com/static/importedfiles/tutorials/MT-003. pdf, 2009.

94. FHWA, *http://ops.fhwa.dot.gov/Freight/sw/index.htm*.

95. Zhang, Z., et al., *Sampling optimization for high-speed weigh-in-motion measurements using in-pavement strain-based sensors.* Measurement Science and Technology, 2015. **26**(6): p. 065003.